ARTICLE

Metal budget and origin of aqueous brines depositing deep-seated Zn-Pb mineralization linked to hydrocarbon reservoirs, North German Basin

Marta Sośnicka[1] · Volker Lüders[1] · Florian Duschl[2] · Dennis Kraemer[3,4] · Oscar Laurent[5,6] · Samuel Niedermann[1] · David A. Banks[7,8] · Franziska Wilke[1] · Cora Wohlgemuth-Ueberwasser[1] · Michael Wiedenbeck[1]

Abstract

The origin, evolution, and interplay of brine and hydrocarbon fluid systems play a crucial role in the formation of deep sediment-hosted base metal ore deposits. Here we investigate ratios of halogens, noble gases, stable C and S isotopes, and metal budgets of aqueous brines, which deposited deep-seated and near-surface hydrothermal Zn-Pb mineralization hosted by Zechstein carbonates in the Lower Saxony Basin (North German Basin), by studies of fluid inclusions in sphalerite and quartz. Major and trace element geochemistry and noble gas isotopic signatures of brine inclusions revealed that the ore-forming fluids were highly reactive and experienced prolonged interactions with host rocks in the constricted, over-pressured metal source regions and consequently evolved from near-neutral, oxidized brines towards more reduced, acidic high-salinity brines. Quartz-hosted halite-saturated fluid inclusions with T_h <200°C contain Zn and Pb concentrations up to ca. 9400 µg g^{-1} and 5200 µg g^{-1}, respectively, and indicate the efficiency of metal scavenging processes. The interactions with Westphalian coals and C_{org}-rich shales influenced the redox state as well as the trace and critical element budget of the sphalerite-hosted fluid inclusions, with enrichment in Ge, Pd, Sb, Tl, Bi, and Ag. The salinities of metalliferous fluids originated primarily from seawater evaporation, however in addition a significant halite-dissolution component is present in the southern part of the Lower Saxony Basin. High concentrations of radiogenic noble gases and potassium in the sphalerite-hosted fluid inclusions are ascribed to strong interactions with the Paleozoic siliciclastic sedimentary pile and crystalline basement rocks. Reflux of the strongly modified, sulfur-poor, Zn-Pb-bearing acidic brines, proceeded via re-activated structurally controlled pathways into sour gas or gas-saturated brine pools in the Zechstein Ca2 carbonate unit. Here, mixing of the ascending metal-rich brines with H$_2$S derived from thermochemical sulfate reduction (TSR), resulted in the deposition of deep-seated Zn-Pb ores in the Lower Saxony Basin. The overall timing of the Zn-Pb ore formation can be constrained to the Upper Cretaceous basin inversion.

Keywords Metalliferous brines · Zn-Pb ore deposits · LA-ICP-MS of fluid inclusions · Noble gases

✉ Marta Sośnicka
marta.sosnicka@gfz-potsdam.de

1   GFZ German Research Centre for Geosciences, Telegrafenberg, D-14473 Potsdam, Germany

2   Technische Universität München, Arcisstraße 21, D-80333 München, Germany

3   Constructor University Bremen (formerly Jacobs University Bremen), Campus Ring 1, D-28759 Bremen, Germany

4   Bundesanstalt für Geowissenschaften und Rohstoffe (BGR) Hannover, Stilleweg 2, D-30655 Hannover, Germany

5   ETH Zürich, Department Erdwissenschaften, Institute for Geochemistry and Petrology, Clausiusstrasse 25, CH-8092 Zürich, Switzerland

6   CNRS, Géosciences Environnement Toulouse, Observatoire Midi-Pyrénées, 14 ave. Edouard Belin, F-31400 Toulouse, France

7   School of Earth and Environment, University of Leeds, Leeds LS2 9JT, UK

8   Department of Geological Engineering, Istanbul University-Cerrahpasha, Istanbul, Turkey

Introduction

Sedimentary basins host a variety of economic base metal deposits worldwide (e.g., stratabound deposits, vein-type deposits, and others) and will be important exploration targets for deep undiscovered mineral resources in the near future. The high exploration potential of deep basins with thick sedimentary cover is demonstrated by discoveries of blind ore deposits in, e.g., Germany, Poland or Australia (Arndt et al. 2017; Nadoll et al. 2019). For example, in the Southern Permian Basin (SPB) in Central Europe, a blind giant world-class Polish Kupferschiefer Cu-Ag ore deposit was accidentally discovered in 1957 during petroleum exploration in the Fore-Sudetic Monocline (Borg et al. 2012). Sediment-hosted base metal deposits are important resources for metals such as Cu, Zn, Pb, Ag, and commonly contain by-products of critical metals: Ga, Ge, In, Co, Pd, Pt, Sb, Au, REE (Leach et al. 2005; Cook et al. 2009; Foltyn et al. 2022), which are of strategic importance (Graedel et al. 2014; Bookhagen et al. 2020). The ever-increasing demand for these metals, due to a transition to a carbon-free economy, drives intensified research efforts to increase successful ore deposit exploration in sedimentary basins worldwide (Hoggard et al. 2020).

Ore-forming processes in sedimentary basins are linked to extensive fluid circulation, which plays a crucial role in re-distribution of base and trace metals within the deep strata. Determining the origin, composition, and migration pathways of fluids in the sediment-hosted ore systems provides better understanding of ore-forming processes from the potential source regions to the sites of ore deposition. Quantitative metal concentrations in fluids pertaining to a specific mineral system can be determined by Laser Ablation-Inductively Coupled Plasma-Mass Spectrometry (LA-ICP-MS) analyses of metal abundances in representative sets of individual fluid inclusions hosted in ore and gangue minerals (Günther et al. 1998; Heinrich et al. 2003; Richard et al. 2011; Pettke et al. 2012; Burisch et al. 2016; Lecumberri-Sanchez et al. 2018). LA-ICP-MS studies of fluid inclusions in sphalerites from sediment-hosted deposits focus on major elements, e.g., Na, K, Cl, Mg, Li, Ca, Mn, Cu, Zn, Pb, Ba, and Sr (Stoffell et al. 2008; Wilkinson et al. 2009; Yardley and Bodnar 2014; Field et al. 2020). Owing to the contamination, caused by the host ore mineral and low elemental abundances, the concentrations of critical trace metals in sphalerite-hosted fluid inclusions have not been studied so far.

In the Lower Saxony Basin (LSB) in NW Germany, several deep-seated Zn-Pb deposits hosted by Zechstein (Ca2) carbonates or metasomatic siderite-(barite) mineralization were accidentally drilled during gas exploration (Duschl et al. 2016; Nadoll et al. 2019; Sośnicka and

Lüders 2019; Knorsch et al. 2020). It has been proposed that the deposition of Zn-Pb ores resulted from mixing of ascending metalliferous brines with hydrogen sulfide, derived by low-temperature thermochemical sulfate reduction (TSR) in Zechstein (Ca2) carbonate gas reservoirs (Sośnicka and Lüders 2019, 2020). Similar Zn-Pb mineralization as well as metasomatic Zn-Fe ores were historically mined near-surface in Zechstein carbonate host rocks at the southern flank of the LSB (Nadoll et al. 2019). Although the source of H$_2$S is unambiguous (Sośnicka and Lüders 2020), the source(s) of metals and their concentrations in ore-forming brines are unknown. To address these knowledge gaps, we determined (i) the concentrations of halogens as well as base and critical metals in individual fluid inclusions, hosted in quartz and sphalerite as well as (ii) element abundances and *in situ* sulfur isotopic compositions of hydrothermal pyrite. Noble gas analyses of sphalerite-hosted fluid inclusions were performed to trace potential fluid source reservoirs, whereas stable carbon isotope analyses of sphalerite-hosted fluid inclusion gases were carried out to constrain the physicochemical conditions of Zn-Pb ore precipitation.

Geological setting

The Lower Saxony Basin (LSB) is the most important gas and oil province in Germany and is one of the several sub-basins of the Southern Permian Basin (SPB) in Central Europe (Fig. 1). The SPB extends in roughly W-E direction from offshore England, the southern North Sea, the Netherlands, northern Germany to the eastern border of Poland (Betz et al. 1987; Kockel 2003; Maystrenko et al. 2008). The basement of the SPB consists of rigid blocks of crystalline rocks of Cadomian to Paleozoic age (Betz et al. 1987). The basin fill comprises Paleozoic to Cenozoic sedimentary rock sequence of thickness reaching up to 12 km in the basin center (Ziegler 1977; Schwab 1985). The evolution of the SPB started in the Late Carboniferous with sedimentation in the foreland basin of the Variscan Orogen and was accompanied by extensional bimodal volcanism (Ziegler 1977; Brink et al. 1992; Benek et al. 1996; Van Wees et al. 2000). The sedimentary conditions changed from marine-paralic to locally terrestrial and led to the formation of thick coal measures which are the major source rocks for gas accumulations in the SPB. The change of the climatic conditions from humid to aridic accompanied by basin subsidence in the Lower Permian, led to increased sedimentation rates and deposition of the siliciclastic Rotliegend red beds with intercalated lacustrine evaporites, especially in the southern North Sea, the Netherlands and northern Germany (Ziegler 1977; Van Wees et al. 2000). In the LSB however, Lower Permian strata was often not preserved (Breitkreuz et al.
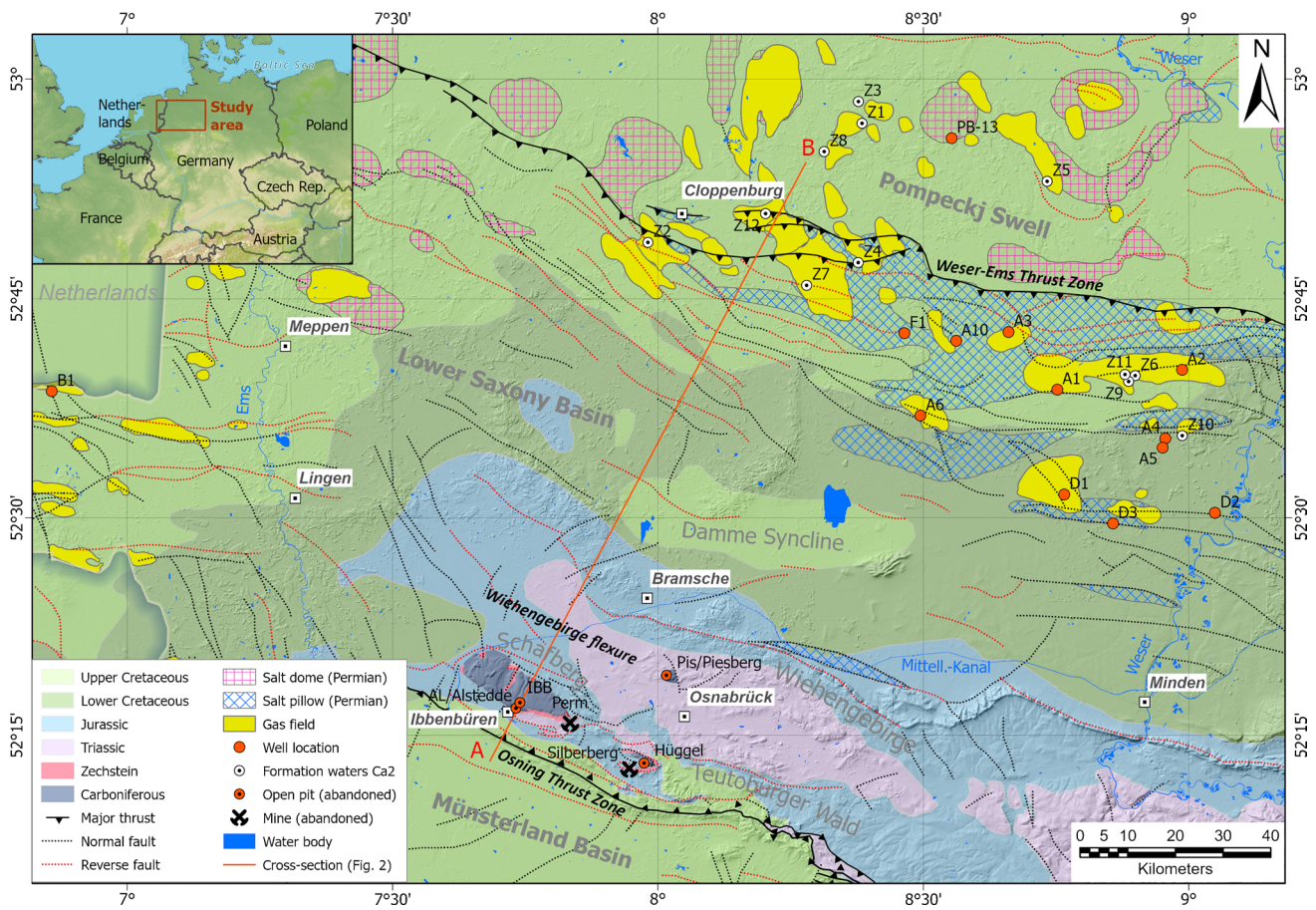
Fig. 1 Simplified geological map of the inverted Lower Saxony Basin and adjacent areas. The LSB is separated by deep-reaching thrust faults from the Münsterland Basin in the south and the Pompeckj Swell in the north. The basin fill experienced significant uplift during basin inversion in the Late Cretaceous to Early Cenozoic with maximum tectonic uplift along the Osning fault zone in the southern part of the basin, locally leading to exhumation of pre-Cretaceous and Paleozoic units, and the formation of distinct mountain ranges such as the Schafberg, Wiehengebirge and Teutoburger Wald. For reasons of clarity, Cenozoic units are neglected in this map. Geology modified after Drozdzewski and Dölling (2018) and Geological Map of Germany 1:1.000.000 (2018); structural features are based on Baldschuhn et al. (2001). Gas fields in Paleozoic and Buntsandstein units after LBEG (2014)

2008) which led to wide-spread unconformable stacking of Zechstein evaporites directly on top of Upper Carboniferous blocks. In the Upper Permian, the marine Zechstein transgression led to thick accumulations of shales, carbonates, sulfates and salt, representing up to seven evaporitic cycles, reaching thickness of up to 2 km in the basin center (Peryt et al. 2010). In the Triassic, the SPB experienced stages of rifting and NNE-SSW striking extension tectonics coupled with differential subsidence of individual tectonic blocks, which led to the onset of halokinetic movements affecting Rotliegend and Zechstein salts (Brink et al. 1992).

During the Middle to Late Jurassic and Late Cretaceous to Paleocene, basin subsidence was interrupted by stages of major uplift (Schwab 1985; Ziegler 1990). During this time, the LSB was formed along large faults of Late Jurassic to Early Cretaceous age during a period of rifting and wrench tectonics (Betz et al. 1987). In the Late Cretaceous

the LSB was uplifted in response to basin inversion. The major Weser-Ems and Osning deep-reaching fault systems (Figs. 1–2), flanking the LSB, were re-activated by NW-SE-striking convergent wrenching, which also involved the basement (Betz et al. 1987). The LSB was partly thrusted over the Münsterland platform along the Osning thrust zone in the south and over the stable Pompeckj Block along the Weser-Ems thrust zone in the north (Schwab 1985; Ziegler 1990). The asymmetric inversion of the LSB resulted in higher uplift rates in the south of the Wiehengebirge flexure-zone (Figs. 1–2), where Upper Carboniferous (Westphalian A-D) as well as Zechstein, Triassic and Jurassic strata were exposed at the surface and developed as the Schafberg (Ibbenbüren), Piesberg and Hüggel positive flower structures (Drozdzewski and Dölling 2018) (Figs. 1–2). In the northern LSB, north of the flexure-zone, uplift was less intense and therefore, the Carboniferous and Zechstein units in this area
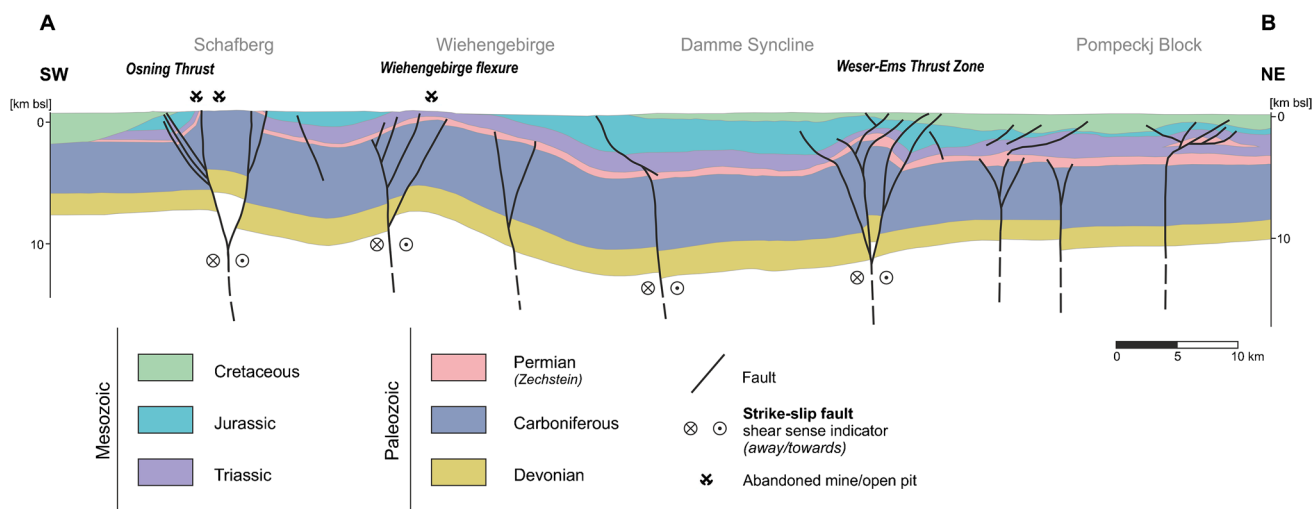
Fig. 2 Geological SW-NE cross-section through the central part of the Lower Saxony Basin (A-B, see Fig. 1) showing some of the most prominent structural features. Many tectonic structures like the Schafberg fault block formed due to uplift along transpressive strike-slip faults, which resulted in exposure of previously deep-seated units of Permian and Carboniferous age (modified after Drozdzewski and Dölling, 2018)

are deeply buried beneath the Mesozoic cover, which has been preserved due to lower erosion rates (Senglaub et al. 2005). The subsequent Laramide phase of the LSB inversion took place in the mid-Paleocene (Betz et al. 1987). The complexity of the tectonic zone centered on the Weser-Ems major fault system is highlighted by numerous flower and pop-up structures, floating tectonic blocks, steep reverse faults, as well as the presence of Zechstein, Triassic, and Jurassic salt layers acting as detachment planes during tectonic movements (Kockel 2003; Schoenherr et al. 2021; Schoenherr and Lüders 2022).

Ores and mineralization in the LSB

Super-deep Zn-Pb mineralization in the central part of the northern LSB hosted by Staßfurt Ca2 gas reservoir carbonate was intersected in several areas during drilling at depths between ~2.7 and 3.6 km. Up to several meter-thick mineralization zones, observed in the drill cores, are hosted by the Ca2 unit or occur at the contact between the Ca2 dolomite and Upper Carboniferous siliciclastic rocks. The ore zones and fracture-fill mineralization are well characterized and consist of sphalerite, galena, pyrite, fluorite and barite (Duschl et al. 2016; Nadoll et al. 2018, 2019; Sośnicka and Lüders 2019; Knorsch et al. 2020). The mineralization in this area coincides with the presence of hydrocarbon and locally prominent CO_2-rich gas reservoirs (e.g., Lüders et al., 2021; Sośnicka and Lüders, 2021).

Near-surface Zn-Pb and Fe ore deposits occur at the hanging wall of the Osning thrust zone and were mined from the Middle Ages until the 19th Century. They are located

in the surroundings of some uplifted Carboniferous blocks, which form horst structures in the Piesberg and Schafberg (Ibbenbüren) areas. Stratabound Zn-Pb ores hosted by the Ca1 Zechstein unit were exploited in the Perm Mine (Fig. 1) from 1861 to 1921. Mineralization is dominated by sphalerite, intergrown with quartz and minor galena. Minor Ag-bearing galena was mined at the Silberberg quarry (Fig. 1) between the twelfth and thirteenth century. Metasomatic brown Zn-Fe ores from the mining areas at the Hüggel and Schafberg contain 36–37% ZnO and 10–24% FeO. The overall production was 4–5 Mt of Fe ore with remaining reserves of 1–3 Mt, and ca. 0.1Mt of Zn+Pb ore (Hagemann 1930; Graupner 1971; Harms 1984; Röhrs 1992).

Sampling and analytical methodology

Sampling strategy

The study area extends from west of the river Weser to north-east of the river Ems (Fig. 1). In the southern, central and western part of the LSB, sampling comprised gangue minerals hosted by Upper Carboniferous strata as well as gangue and Zn-Pb ores hosted by Zechstein carbonates. This sampling strategy allows tracing migration pathways of ore-forming fluids, which were ascending from depth through the Upper Carboniferous strata into the overlying Zechstein carbonate. Samples were collected from drill cores between depths of 2.8–4.6 km (Upper Carboniferous unit) and 2.9–3.6 km (Zechstein Ca2 unit). These drill cores originate from deep wells, which were sunk in the central and western part of the LSB and close to the Pompeckj Block (PB)/LSB

border zone during hydrocarbon exploration. The sample material comprises fracture-fillings with barren quartz, carbonate and locally minor barite hosted by Upper Carboniferous siliciclastic rocks as well as Zn-Pb mineralization, fluorite, calcite and hydrothermal pyrite from Zechstein Ca2 carbonate. The deep-seated massive and vein Zn-Pb mineralization studied by Sośnicka and Lüders (2019) were used for the determination of trace and critical metal concentrations in individual sphalerite-hosted fluid inclusions as well as for bulk stable carbon isotope and noble gas analyses. In the southernmost LSB, sampling was carried out from outcrops south of Bramsche: Piesberg, Alstedde/Schafberg, Ibbenbüren and mine dumps of the former Perm mine (Fig. 1).

Microthermometry

Microthermometric measurements of fluid inclusions hosted in quartz were performed at GFZ Potsdam, Germany, using a FLUID INC. adapted USGS heating-freezing system mounted on a BX50 Olympus microscope. The USGS stage was calibrated with synthetic Synflinc fluid inclusion standards. The precision is $\pm 0.1°C$ for T_m(ice) and $\pm 1.7°C$ for $T_h > 350°C$. Salinities of aqueous fluid inclusions were calculated from corresponding T_m(ice) and T_m(hydrohalite) values using the HOKIEFLINCS_H$_2$O-NaCl spreadsheet (Sterner et al. 1988; Bodnar 1993; Steele-MacInnis et al. 2012).

EPMA

Element concentrations in sphalerite and pyrite were measured at GFZ Potsdam, Germany, using a field-emission JEOL Hyperprobe JXA 8500F. The conditions for the electron probe-microanalysis conducted in the wavelength-dispersive mode are 20 keV, 20 nA at a beam size of ca. 0.5 μm. Quantitative analyses were determined by calibrating with natural pentlandite (Fe, Ni, S), sphalerite (Zn), galena (Pb), rhodonite (Mn) and pure metals for Cd, Cu, Ga, Ge, and Te. Counting times on the peak varied between 10s, 20s, and 40s with corresponding backgrounds collected in half of the peak acquisition time. Data reduction was done using a ZAF correction, both taking into account the interactions between incident electrons and the target (Z), between the generated photons and the matrix (A) as well as the fluorescence (F). Under these conditions, detection limits are 0.05 wt% for Zn, 0.03 wt% for Fe, Pb and Ge, and ≤0.02 wt% for all other elements. The relative analytical error depends on the absolute abundances of each element and is estimated to be <1% at the ≥10 wt% level, ≤10% down to the 1 wt% level and ≤20% down to the 0.2 wt% level. Back-scattered electron (BSE) and qualitative element distribution maps were also obtained by means of the microprobe. The latter was done for pyrite using 20 keV, 20 nA with 1 μm probe size on 1 μm intervals

and a short 300 ms dwell time. The Pb (Mα) X-ray line using a PETH crystal was applied to scan the pyrite.

LA-ICP-MS analyses of fluid inclusions

Analyses of individual fluid inclusions in quartz were performed by laser ablation-inductively coupled plasma-quadrupole mass spectrometry (LA-ICP-Q-MS) at ETH Zürich, Switzerland. Analysis utilized an excimer (ArF; 193-nm wavelength) Compex Pro 102F laser ablation system (Coherent, Germany) coupled to a Nexion2000 (PerkinElmer, USA/Canada) fast-scanning quadrupole ICP-MS as described in Laurent et al. (2021). An in-house built glass ablation cell with a volume of ca. 6 cm^3 was used. To minimize gas blanks, the ablation cell was polished using 1-μm alpha-alumina suspension (Struers, Denmark) and further cleaned with Aqua Regia prior to the analysis. In addition fluorinated ethylene propylene (FEP) tubing (Rotilabo®, Carl Roth GmbH, Germany) was used for gas and aerosol transport (see Schlöglova et al., 2017) to minimize the blank signal.

A laser pulse rate of 10 Hz was selected for all analyses and a spot diameter of 40 μm for reference materials. The spot diameter used for fluid inclusions ranged from 10 to 100 μm depending on the individual inclusion size and was adjusted so as to completely ablate the inclusion using a manually opening iris aperture. We used a laser output energy of ca. 60 mJ for reference materials and ca. 150 mJ for quartz-hosted fluid inclusions (energy density of ca. 20 J cm^{-2}). The carrier gas consisted of 0.9 L min^{-1} of 5.0 grade He, which was combined with 1.05–1.10 L min^{-1} of 6.0 grade Ar make-up gas downstream of the ablation cell. No signal homogenization device was used to ensure as fast washout as possible and representative recording of the fluid inclusion signals.

The ICP-MS was operated in standard mode (no collision cell gas used) and optimized for maximum sensitivity on the whole mass range, a U/Th ratio of ca. 1 and a low oxide formation ratio (≤ 0.5 % ThO$^+$/Th$^+$) on laser mode. The following element menu: ^{7}Li, ^{11}B, ^{23}Na, ^{24}Mg, ^{27}Al, ^{29}Si, ^{31}P, ^{34}S, ^{35}Cl, ^{39}K, ^{43}Ca, ^{55}Mn, ^{57}Fe, ^{59}Co, ^{62}Ni, ^{63}Cu, ^{66}Zn, ^{69}Ga, ^{71}Ga, ^{73}Ge, ^{75}As, ^{77}Se, ^{79}Br, ^{85}Rb, ^{88}Sr, ^{89}Y, ^{95}Mo, ^{101}Ru, ^{103}Rh, ^{105}Pd, ^{107}Ag, ^{111}Cd, ^{118}Sn, ^{121}Sb, ^{125}Te, ^{133}Cs, ^{137}Ba, ^{195}Pt, ^{197}Au, ^{202}Hg, ^{205}Tl, ^{208}Pb, and ^{209}Bi, was used. Dwell times were set to 1 ms for all elements except Au (10 ms) and quadrupole settling times to 0.2 ms, resulting in a total sweep time of 62 ms (see Laurent et al. 2021 for details about the merits when using short settling and sweep times).

The LA-ICP-MS signals were processed with the Matlab-based program SILLS (Guillong et al. 2008) with limits of detection calculated following Pettke et al. (2012). The fluid inclusion data have been revised for falsely positive numerical values, i.e., only signals that have clearly visible fluid inclusion peak rising statistically above host

background were considered for calculations. All analyses were calibrated against the external standard NIST SRM 610 (Jochum et al. 2011), except the S, Cl and Br contents that were calibrated using Sca-17 scapolite (Seo et al. 2011). The stoichiometric Si content of quartz was used as internal standard for matrix correction. Absolute concentrations of trace elements in fluid inclusions were obtained by referencing element ratios against the salinity (wt% NaCl equiv.) determined by microthermometry on the respective individual inclusion as internal standard, or the average value for a given fluid inclusion assemblage (FIA).

Fluid inclusions hosted in sphalerite were analyzed at GFZ Potsdam, Germany using a Geolas Compex Pro 193 nm excimer laser coupled to a Thermo iCAP Triple Quad ICP-MS. Each analysis consisted of 30s background measurement, varying analytical time (laser on) depending on depth and size of the inclusions and 15s wash-out. Analytical conditions included a laser energy density of 14 J cm^{-2}, repetition rate of 5 Hz and constant spot diameters of 24, 32, 44, 60, 90, and 120 μm. The ICP-MS was operated in normal on-mass mode and the gas cell was not used. The following element list was used: ^{7}Li, ^{11}B, ^{19}F, ^{23}Na, ^{24}Mg, ^{29}Si, ^{31}P, ^{32}S, ^{34}S, ^{35}Cl, ^{39}K, ^{42}Ca, ^{44}Ca ^{55}Mn, ^{57}Fe, ^{59}Co, ^{60}Ni, ^{63}Cu, ^{66}Zn, ^{67}Zn, ^{69}Ga, ^{71}Ga, ^{70}Ge, ^{73}Ge, ^{75}As, ^{77}Se, ^{85}Rb, ^{95}Mo, ^{101}Ru, ^{103}Rh, ^{105}Pd, ^{111}Cd, ^{115}In, ^{118}Sn, ^{121}Sb, ^{125}Te, ^{133}Cs, ^{137}Ba, ^{195}Pt, ^{197}Au, ^{202}Hg, ^{205}Tl, ^{208}Pb, and ^{209}Bi. Dwell times were set to 10 ms for all elements except Se, Pt, Au (20 ms). NIST 610 was used as external standard. Concentrations of all trace metals in fluid inclusions were checked manually before the data processing in SILLS software. Zn concentrations measured in sphalerites using WDS-EPMA were used for internal matrix correction, whereas salinities of sphalerite-hosted fluid inclusions (wt% NaCl equiv.) determined by microthermometry were used as internal standard.

Crush-leach analysis of fluid inclusions

Bulk crush-leach analysis of fluid inclusions was carried out at the University of Leeds following the methodology described in detail by Banks et al. (2000). Samples were crushed to a 1–2mm grain size and cleaned by boiling several times in 18.2 MΩ water. Subsequently, the cleaned samples were dried and approximately 0.5 to 1 g of purified sample material was manually crushed with an agate mortar and pestle. The resulting mineral powder was leached with 18.2 MΩ water and filtered through a 0.2-μm nylon mesh prior to analysis. Ion chromatography was used for analysis of the anions Cl, Br, and SO$_4$ in the leachate solutions and flame emission spectroscopy for the determination of Na and K. Precision of the analyses, from replicate analysis, is better than 5% RSD.

Noble gas analysis

Noble gas analysis was conducted at GFZ Potsdam, where samples of 0.2–1.5 g were loaded individually into an ultra-high vacuum crusher, which was evacuated for at least 24 h at room temperature. After a blank measurement to ensure there was no leak, gases were extracted from fluid inclusions by crushing the mineral grains between two metal jaws. The released gases were removed in two Ti sponge and two SAES (ZrAl) getters before the heavy noble gases Ar, Kr, and Xe were adsorbed onto a stainless-steel frit at 50 K and the light noble gases He and Ne onto charcoal at 11 K. After sequential release, He, Ne, Ar, and Kr+Xe were admitted separately into a VG5400 mass spectrometer for the determination of noble gas concentrations and isotopic compositions (except for Kr isotopic compositions and ^{124}Xe, ^{126}Xe). With one exception (sample A4-84), the total analytical blanks (in units of cm^3 STP) measured prior to each sample gas extraction were (2–4) × 10^{-12} for ^{4}He, (1–5) × 10^{-12} for ^{20}Ne, (4–25) × 10^{-10} for ^{40}Ar, (8–28) × 10^{-14} for ^{84}Kr, and (3–21) × 10^{-14} for ^{132}Xe, with atmospheric isotopic compositions. For A4-84 the blanks were higher by an order of magnitude, but still negligible compared to the sample gases, except for Xe (blank contribution ~5%). The mass spectrometer sensitivity and the isotopic mass discrimination were determined using the GFZ lab standard, an artificial mixture of the five noble gases with a ^{3}He/^{4}He ratio of (15.58±0.17) R$_A$ (where R$_A$ is the atmospheric ^{3}He/^{4}He of 1.39×10^{-6}) and atmospheric isotopic compositions for Ne, Ar, Kr and Xe. Details about analytical procedures and data reduction methods can be found in Niedermann et al. (1997). All data have been corrected for analytical blanks, isobaric interferences (^{40}Ar^{++}, CO$_2$$^{++}$, H^{35}Cl^{+}, H^{37}Cl^{+}), and mass discrimination effects.

Formation water analysis

Formation water samples from free water knockout separators (FWKO samples; production waters that may have been affected by condensate dilution) were collected by EMPG from twelve different Zechstein production wells in the LSB. The samples were stored in clean glass bottles and immediately transported to the Geochemistry Lab of Constructor University Bremen where residual oil was removed from the formation water with the help of a separatory funnel. The water samples were filtered with a Sartorius filter tower using 0.2 μm filter cellulose acetate membrane filters and afterwards acidified with suprapure HCl to a pH of 2 for stabilization. The formation water samples were measured with a Spectro Ciros Vision SOP ICP-OES.

Stable carbon and sulfur isotopes

Individual mineral separates of sphalerite, quartz, fluorite, and barite-calcite, consisting of 1–4 mm grains hosting fluid inclusions, were prepared for bulk isotope analysis of fluid inclusion gases at GFZ Potsdam, Germany. The stable carbon isotopic compositions of CO_2 and CH_4 gases in fluid inclusions were acquired using a sample crusher connected via a gas chromatography column to an elemental analyzer isotope ratio mass spectrometry system. This analytical setup allows online simultaneous measurements of stable isotope ratios of N_2, CH_4, and CO_2 in natural gas mixtures released by crushing of fluid inclusions. The analytical procedure and its reproducibility are described in detail by Lüders et al. (2012), Plessen and Lüders (2012), and Sośnicka and Lüders (2020).

A Cameca 1280-HR SIMS instrument at the GFZ Potsdam was used to conduct *in situ* $\delta^{34}S$ determinations on <20 µm domains in pyrite crystals, employing a slightly modified analytical design where particularly high spatial resolution was required. Instrument calibration was based on the Balmat pyrite RM, which has an assigned value of $\delta^{34}S_{CDT} = 15.1$ (Crowe and Vaughan 1996). The absolute value for the zero-point on the $\delta^{34}S_{CDT}$ was set at $^{34}S/^{32}S = 0.044163$ based on the recommendation by Ding et al. (2001), yielding an absolute $^{34}S/^{32}S = 0.044830$ for the Balmat pyrite reference sample. The repeatability of determinations was better than ±0.1‰ (1σ) for our analytical set-up. Based on these observations, our data are reliable to better than ±0.2‰ (1σ) in terms of differences between individual determinations. Our absolute data accuracy is limited only by the roughly 1‰ variability which has been reported for the Balmat RM standard (Whitehouse 2013). The SIMS analytical method is reported in detail in Online Resource 1.

Results

Fluid inclusion petrography and microthermometry

In general, fluid inclusions in gangue minerals hosted by Upper Carboniferous strata and Zechstein carbonate in the LSB represent two compositional types. These are type I aqueous 2-phase inclusions (liquid + vapor) and type II gas-rich inclusions that contain gas mixtures of variable compositions. Type I inclusions may occasionally contain a halite daughter crystal or accidentally trapped solids (sulfates, carbonates), but only representative 2-phase (L+V) inclusions were considered in this study. Quartz and carbonate fracture-fillings in Upper Carboniferous rocks commonly host CH_4-$CO_2\pm N_2$ type II inclusions. In contrast, type II inclusions in calcite, fluorite or anhydrite

mineralization in Zechstein Ca2 carbonate predominantly contain CH_4-CO_2-$H_2S\pm N_2$ gas mixtures (Sośnicka and Lüders 2020, 2019; Lüders et al. 2021). Previously studied type I fluid inclusions, hosted in early quartz I and younger quartz II from the Piesberg quarry (Upper Carboniferous strata) differ from each other not only in terms of salinity and temperature, but also in gas composition. It has been shown that type II CH_4-CO_2 gaseous inclusions in early quartz I are CH_4-rich, whilst gas inclusions (type II) in younger quartz II have CO_2-$CH_4\pm N_2$ compositions (Lüders et al. 2012; Wüstefeld et al. 2017).

Petrographic observations of fluid inclusions and microthermometric data from the southern as well as central LSB are presented in Figs. 3 and 4, and in Online Resource 2.

Southern LSB

Quartz intergrown with sphalerite from the Perm Mine (Fig. 3e–f) as well as quartz fracture fillings from uplifted Upper Carboniferous blocks (Fig. 3a–d), adjacent to the overlying mineralized Zechstein Ca1 unit from different localities in the southern part of the LSB (Piesberg, Alstedde/Schafberg, Ibbenbüren, Perm Mine areas) were studied for fluid inclusions.

Primary type I and type II inclusions often occur together within an individual quartz crystal and are arranged along well-defined growth zones (Fig. 3a–b), suggesting co-genetic entrapment within an immiscible system. Closely spaced crack-seal growth zones are also decorated by primary type I inclusions (Fig. 3c–d). Pseudosecondary inclusions follow short trails, which terminate within individual crystals and do not reach their boundaries. This indicates that these inclusions were entrapped while the crystal was still growing. The microthermometric data of type I aqueous fluid inclusions in fracture-filling quartz from Upper Carboniferous strata plot into two distinct groups, hereafter named: A and B (Fig. 4). The overall ranges of homogenization (LV→L) temperatures (T_h) and salinities for group A fluid inclusions are: 181–288°C (median: 245°C) and 12.4–20.4 wt% NaCl equiv. (median: 16.6 wt% NaCl equiv.), respectively. In contrast, group B inclusions show lower T_h of 140–208°C (median: 189°C) and higher salinities of 22.6–27.5 wt% NaCl equiv. (median: 25.1 wt% NaCl equiv.) (Fig. 4, Online Resource 2). It is worth noting that one of the highest T_h ranges (259–264°C) were yielded by group A primary inclusions in crack-seal growth zones in quartz fracture-fillings hosted by Upper Carboniferous sandstone (Fig. 3c–d, Online Resource 2). A few measured pseudosecondary FIA's show similar microthermometric data as primary fluid inclusions (e.g., in sample KA-18-3, Online Resource 2) suggesting that they were entrapped from the same fluid.

Fig. 3 Microphotographs of primary quartz-hosted fluid inclusions from the southern (**a–f**) and central (**g–h**) parts of the Lower Saxony Basin. **a–b** growth zones in euhedral fracture-filling quartz (qtz) decorated by co-existing primary aqueous 2-phase (L+V) inclusions and gas (G) inclusions, Piesberg area (sample PH-1). **c** fluid inclusion-rich crack-seal growth zones (red arrows) oriented perpendicularly to the quartz crystal face, Piesberg area (sample KA-6). **d** primary aqueous 2-phase (L+V) inclusions entrapped along parallel spaced crack-seal growth zones, Piesberg area (sample Pis1-4). **e** sphalerite (sp) ore intergrown with elongated quartz crystals, Perm Mine (sample Perm-4). **f** primary 2-phase (L+V) quartz-hosted aqueous fluid inclusions in growth zones, in elongated quartz intergrown with sphalerite ore from the Perm Mine; the field of view is also shown as stippled white line-contoured box in **e**. **g–h** fracture-filling quartz crystals showing dark cores rich in gaseous inclusions and bright rims containing aqueous 2-phase (L+V) brine inclusions (black arrow in **h**), central part of the LSB (sample D1-7)
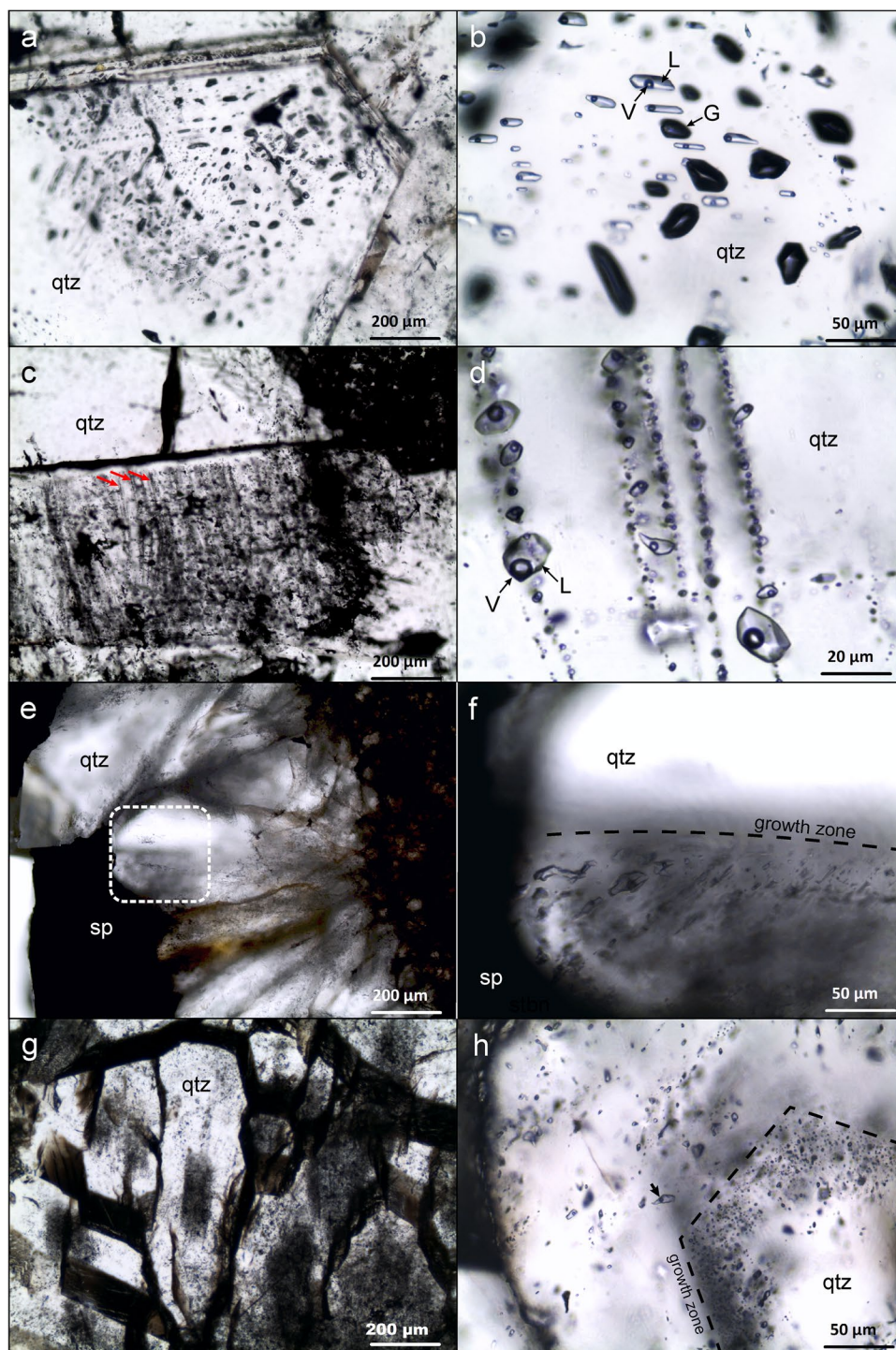
In the Piesberg area, FIA's were studied in two generations of quartz fracture-fillings in the uplifted Upper Carboniferous blocks. Group A aqueous inclusions (type I), which are associated with type II gas inclusions in the early quartz I generation, show the highest T_h of up to 288°C and the lowest salinities of 12.4–19.6 wt% NaCl equiv. (PH-2, Pis1, KA-6, KA-11, KA-17, KA-18 in Fig. 4). In contrast, group B aqueous inclusions, which show lower T_h of 183–205°C and higher salinities of 22.6–27.5 wt% NaCl equiv., are hosted in younger quartz II (PH-1, Pis3-2 in Fig. 4). In the Ibbenbüren area and in the Upper Carboniferous black coal mine, group A aqueous inclusions show median T_h = 234°C and salinity of 15.7 wt% NaCl equiv. (BU-Pr in Fig. 4), as well as median T_h = 209°C and salinity of 18.9 wt% NaCl equiv. (IBB in Fig. 4), respectively.
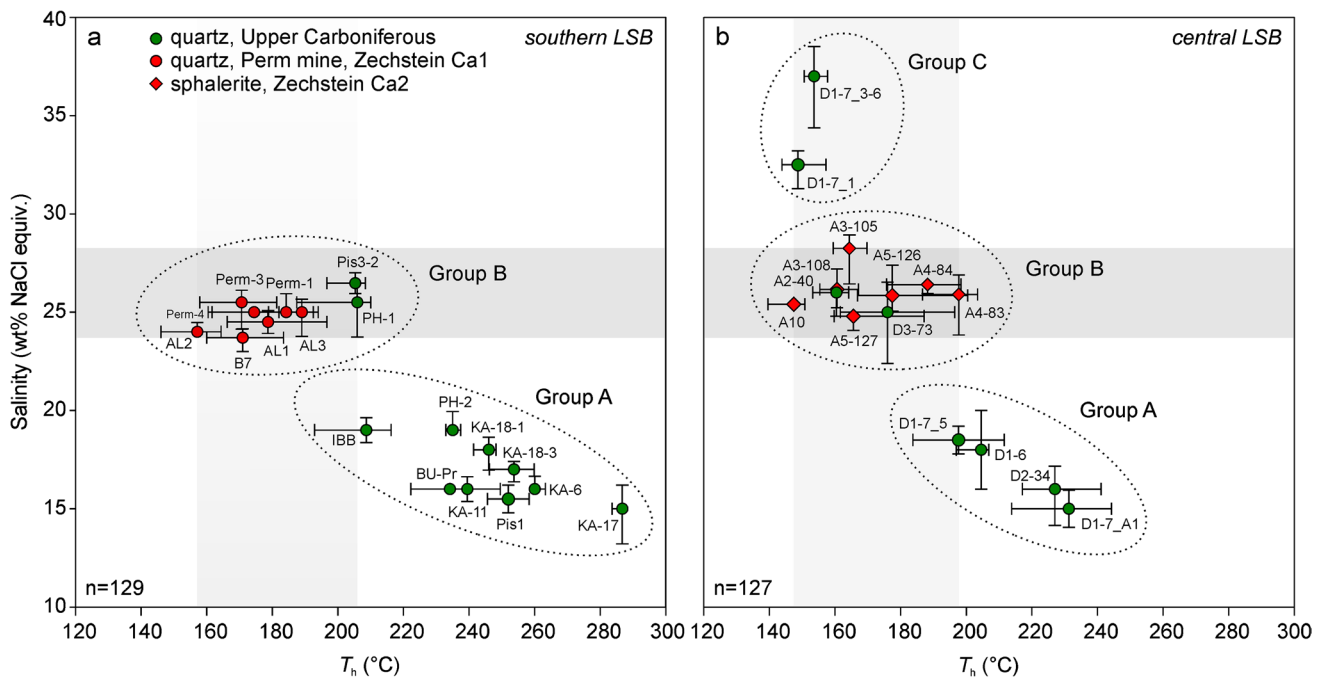
Fig. 4 Bivariate diagrams showing median values and ranges of homogenization temperatures and salinities of fluid inclusions hosted in fracture-filling quartz from Upper Carboniferous and Zechstein strata, as well as in quartz intergrown with Zn-Pb ore from the Perm Mine. **a-b** data clusters into three distinctive groups: A, B and C. Microthermometric data of high-salinity fluid inclusions, hosted in sphalerite from deep-seated Zechstein Ca2 mineralization from the central LSB (Sośnicka and Lüders 2019), are shown for comparison in **b**. The error bars represent standard deviation, whereas symbols are median values. Microthermometric data from fluid inclusion assemblages (FIA's) in each measured sample show high consistency

All primary type I FIA's hosted in quartz fracture-fillings and quartz from sphalerite ore in Zechstein Ca1, show microthermometric characteristics akin to group B (Fig. 4). Quartz crystals from Alstedde/Schafberg (AL1-3, B7) contain primary group B aqueous inclusions showing high salinities of 23.2–26.1 wt% NaCl equiv. and T_h of 140–200°C (median: 171°C; Fig. 4). Primary group B fluid inclusions hosted in elongated quartz, intergrown with Ca1 hosted Zn ore from the Perm Mine (Fig. 3f), show a salinity range between 23.6 and 26.1 wt% NaCl equiv. (median: 25 wt% NaCl equiv.) and T_h values of 145–196°C (median: 177°C, Fig. 4), which is similar to the range of salinity and T_h values of group B inclusions in the younger, Upper Carboniferous-hosted, fracture-filling quartz II from Piesberg (PH-1, Pis3-2 in Fig. 4).

Central LSB

In the central part of the LSB, the fracture-fill quartz samples were collected from four deep wells sunk into Upper Carboniferous siliciclastic rocks overlain by mineralized Zechstein Ca2 carbonate. The quartz crystals often show prominent growth zones decorated with primary fluid inclusions. The crystal cores are clustered with dark type II gaseous inclusions (Fig. 3g–h) in contrast to the outer growth zones, which are decorated with type I 2-phase aqueous (L+V) inclusions (Fig. 3g–h). Group A FIA's show high T_h of 188–256°C (median: 228°C) and low salinities of 12.6–19.8 wt% NaCl equiv. (median: 16.1 wt% NaCl equiv.). These ranges and median values are similar to those of group A inclusions from the southern LSB (Fig. 4). There is no significant difference between the median T_h and salinity values of primary (225°C, 16.7 wt% NaCl equiv.) and pseudo-secondary (229°C, 15.3 wt% NaCl equiv.) group A inclusions. Primary group B fluid inclusions show T_h values between 148 and 205°C (median 162°C), and salinities of 19.4–26.5 wt% NaCl equiv. (median: 25.6 wt% NaCl equiv.). The lowest T_h values (145–162°C, median: 153°C) and extremely high salinities (31.4–39.1 wt% NaCl equiv., median: 34.4 wt% NaCl equiv.) were measured in primary fluid inclusions, named as group C.

Two generations of aqueous fluids of strikingly contrasting salinities and temperatures were observed in outer growth zones of sample 7 from well D1 (Fig. 4). The lower salinity (12.6–18.6, median: 15.2 wt% NaCl equiv.) fluid inclusions in this sample (D1-7_A1, D1-7_5 in Fig. 4) show high T_h of 188–256°C (median: 229°C), which are typical of group A inclusions, whereas significantly lower T_h values are typical of the high-salinity group C aqueous brines (D1-7_3-6, D1-7_1 in Fig. 4). Fluid inclusions having lower

salinities (group A) often form pseudo-secondary trails, whereas high-salinity inclusions (group C) occur within small, restricted clusters. The timing relationship between these two aqueous inclusion types occurring within the same sample is difficult to constrain.

Element abundances in fluid inclusions

Variable contents of metals, halogens, and trace elements were detected in selected fluid inclusion suites (Online Resource 3). Concentrations of the most abundant metals in the inclusions hosted in quartz fracture-filling minerals from Upper Carboniferous rocks as well as quartz and sphalerite mineralization from Zechstein (Ca1, Ca2) units are shown in Figs. 5–6, 7a, 8.

Fracture-filling quartz from the southern LSB

Group B aqueous inclusions hosted in quartz intergrown with sphalerite from the Perm Mine have the highest Zn concentrations of 201–9491 µg g^{-1} (median: 1354 µg g^{-1}) in the LSB (Fig. 5). Similar magnitudes of Zn concentrations of 618–3408 µg g^{-1} (median: 2029 µg g^{-1}) are observed in group B FIA's hosted in younger quartz II from Upper Carboniferous strata in the Piesberg area. In contrast, group A FIA's in early quartz I from the Piesberg area have significantly lower Zn concentrations between 100 and 1471 µg g^{-1} (median: 406 µg g^{-1}) (Fig. 5). The lowest Zn contents of 26–237 µg g^{-1} (median: 52 µg g^{-1}) were measured in group

A fluid inclusions in quartz from the Upper Carboniferous in the Ibbenbüren area, and in group B inclusions from Zechstein-hosted quartz in the Alstedde/Schafberg areas (21–1220 µg g^{-1}, median: 133 µg g^{-1}). Concentrations of Pb, Fe, Mn and Ba show overall trends similar to Zn, whereas Cu has lower and more homogeneous concentrations (1–157 µg g^{-1}, median: 8 µg g^{-1}) irrespective of the location (Fig. 5). Quartz-hosted FIA's also have high concentrations of Li, B and Sr, having the highest median concentrations among all detected trace elements (Fig. 8). Trace element patterns for fluid inclusions from Upper Carboniferous and Zechstein Ca1 strata are consistent (Fig. 8). However concentrations are higher in the Upper Carboniferous unit except for Li and Tl.

Fracture-filling quartz from the central LSB

The highest Zn concentrations of 509–9201 µg g^{-1} (median: 3348 µg g^{-1}) were measured in group C brine FIA's in quartz from well D1 (Fig. 6). Group A FIA's from the same well have lower Zn contents of 584–2313 µg g^{-1} (median: 1183 µg g^{-1}). Zn concentrations in group B fluid inclusions from wells D3 and A2 are 339–861 µg g^{-1} (median: 591 µg g^{-1}) and 199–2377 µg g^{-1} (median: 458 µg g^{-1}), respectively. Local relative enrichment in Fe is observed in group B FIA's from well D3 (702–8136 µg g^{-1}, median: 4551 µg g^{-1}) and group C brines from well D1 (923–7691 µg g^{-1}, median: 2519 µg g^{-1}) (Fig. 6). Cu contents of 1–187 µg g^{-1} (median: 10 µg g^{-1}) in fluid inclusions do not show any consistent relation across

Fig. 5 Diagram combining: **a** median salinity and homogenization temperature data of quartz-hosted fluid inclusion assemblages (FIA's) with **b** median concentrations of metals: Zn, Pb, Cu, Ba, Fe, and Mn in these FIA's. Samples are from Upper Carboniferous and Zechstein Ca1 strata in the Ibbenbüren, Piesberg and Alstedde/Schafberg areas, and the Perm Mine, situated in the southern part of the Lower Saxony Basin. Error bars show standard deviation. Where error bars are not shown they are equal to or smaller than the symbol size. Data of individual FIA's are separated using white and grey vertical fields
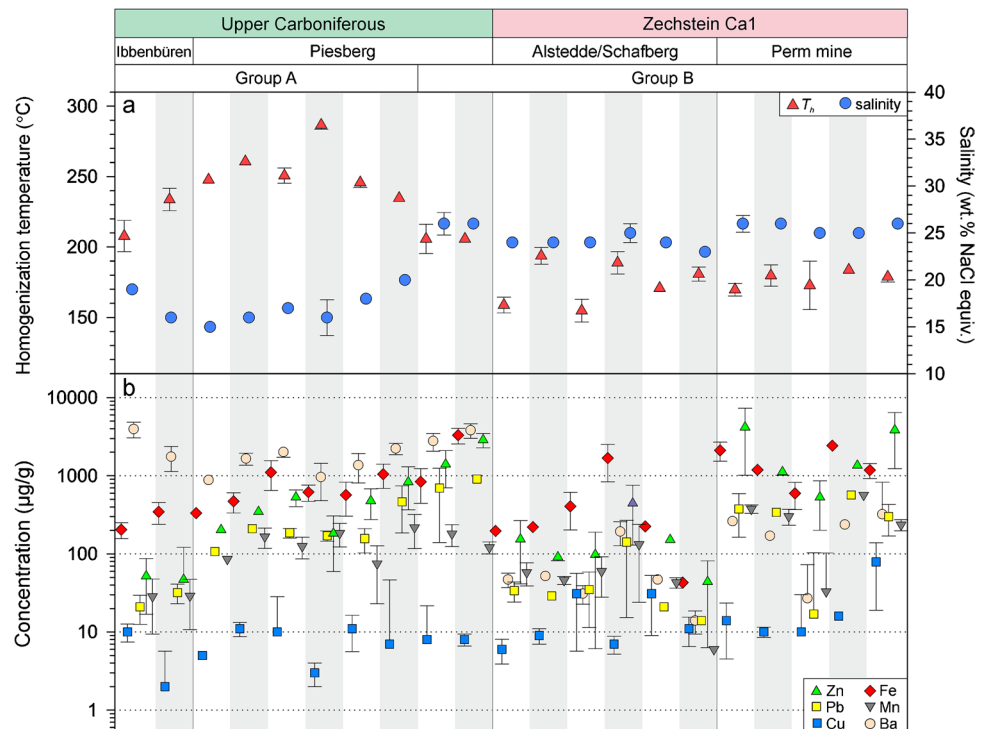
Fig. 6 Diagram combining: **a** median salinity and homogenization temperature data of quartz-hosted fluid inclusion assemblages (FIA's) with **b** median concentrations of metals: Zn, Pb, Cu, Ba, Fe and Mn in these FIA's. Samples are from Upper Carboniferous and Zechstein Ca2 strata, intersected in deep wells: A2, A4, A5, A6, A10, B1, D1, D2, D3, in the central part of the northern flank of the Lower Saxony Basin. Error bars show standard deviation. Where error bars are not shown they are equal to or smaller than the symbol size. Data of individual FIA's are separated using white and grey vertical fields
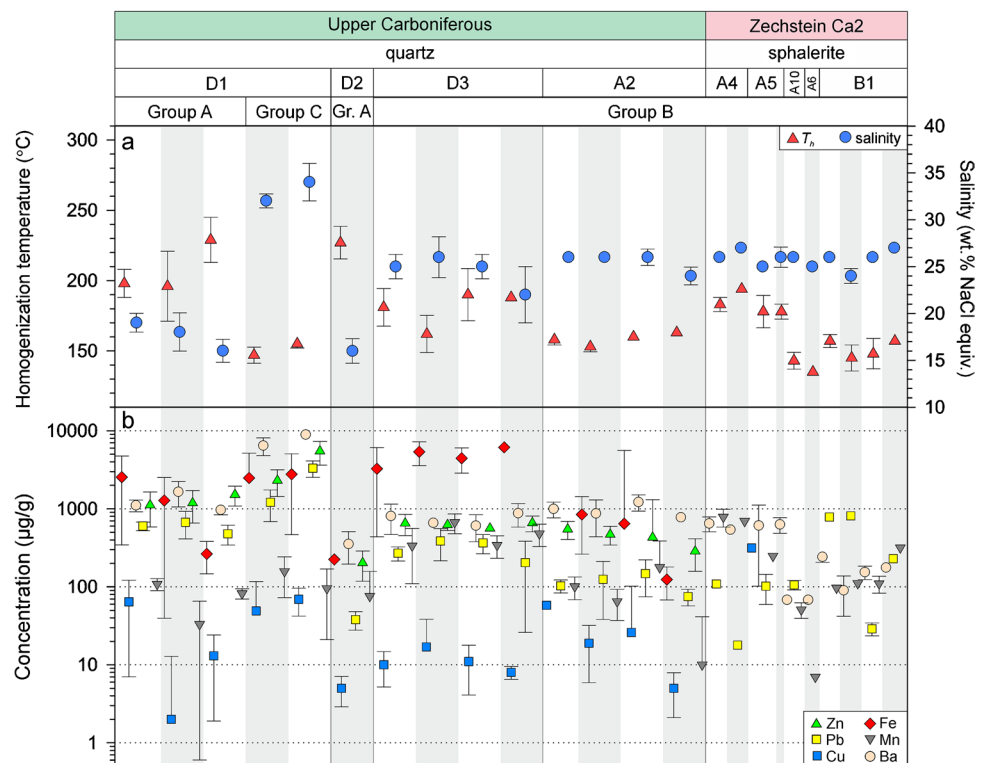
the studied wells (Fig. 6). The lowest Zn concentrations were recorded in group A inclusions from well D2 (100–307 μg g⁻¹, median: 203 μg g⁻¹). Pb, Ba and Mn generally mimic trends consistent with Zn, in contrast to more variable concentrations of Fe and Cu (Fig. 6). Median trace element concentrations in quartz-hosted fluid inclusions from the central part of the LSB have very similar patterns to analyses from the southern LSB, with exception that they are slightly higher for the majority of trace elements, e.g., Ge, Pd, Cd or Sb (Fig. 8).

Sphalerite ores from the western and central LSB

Elemental analyses show that sphalerite-hosted fluid inclusions contain detectable concentrations of critical and trace metals such as Li, Ge, Sr, Pd, In, Sb, Bi and B, Mn, As, Rb, Ag, Cs, Ba, Tl, and Pb. Concentrations of these metals are presented in the Figs. 7–8, and Table 1 in Online Resource 1. Sphalerites from the central part of the LSB show more diversity in element abundances in fluid inclusions compared to sphalerites from the western part of the LSB where elements such as As, Ga, Pd, Ag or Bi were not detected. Pb concentrations in sphalerite-hosted inclusions are relatively low and vary between 18 and 814 μg g⁻¹ (median: 109 μg g⁻¹). Germanium locally shows elevated concentrations of up to 1194 μg g⁻¹; however, the median concentration is 59 μg g⁻¹ (Fig. 7). Fluid inclusions have elevated contents of Li (86–846 μg g⁻¹, median: 297 μg g⁻¹), B (21–1883 μg g⁻¹, median: 257 μg g⁻¹), Sr (1078–8342 μg g⁻¹, median: 2789

μg g⁻¹), Ba (64–1199 μg g⁻¹, median: 501 μg g⁻¹) and Tl (0.1–4953 μg g⁻¹, median: 2 μg g⁻¹) (Fig. 7). Concentrations of Ga (4–5 μg g⁻¹), As (4–45 μg g⁻¹), Rb (9–77 μg g⁻¹), Pd (0.05–0.9 μg g⁻¹), Ag (3–41 μg g⁻¹), In (1–15 μg g⁻¹), Sb (1–92 μg g⁻¹), Cs (3–49 μg g⁻¹), and Bi (0.1–0.4 μg g⁻¹) are comparatively lower (Fig. 7).

Formation waters

Formation waters from Zechstein Ca2 carbonate reservoirs at the northern flank of the central part of the LSB show elevated sulfur concentrations (108–7465 μg g⁻¹, median: 780 μg g⁻¹). In contrast, metal concentrations, e.g., Cu (0.08–0.13 μg g⁻¹), Zn (1.3–1.5 μg g⁻¹), Fe (0.21 μg g⁻¹), Mn (0.2–85.7 μg g⁻¹) are very low (Online Resource 4). Formation waters are also enriched in B, Li, Br, Ca, K, Mg, Sr (medians: 166 μg g⁻¹, 82 μg g⁻¹, 779 μg g⁻¹, 24961 μg g⁻¹, 1839 μg g⁻¹, and 151 μg g⁻¹, 19 μg g⁻¹, respectively).

Stable carbon and sulfur isotopes

The stable carbon isotope analyses of fluid inclusion gases in sphalerites and fracture-filling minerals are presented in Table 1, and Figure 1 in Online Resource 1. The δ¹³C$_{CH4}$ and δ¹³C$_{CO2}$ ratios of fluid inclusion gases hosted in sphalerites from the central and southern LSB range between −26.0 and -6.4‰, and between -9.0 and -1.4‰, respectively. Fluid inclusion gas in quartz that is intergrown with

Fig. 7 Element abundances in sphalerite-hosted fluid inclusions and sphalerite hosts from deep wells in the Lower Saxony Basin.
a Vertical box plots with error bars showing ranges and median concentrations of critical (in bold, dark grey) and trace metals in sphalerite-hosted fluid inclusions, wells A3, A4, A5, A6, A10, B1.
b Vertical box plots with error bars showing ranges and median concentrations of elements in sphalerite crystals from wells A4, A5 and B1. Open circles indicate outliers (data from Knorsch et al. 2020).
c–d Time-resolved laser ablation spectra for fluid inclusions hosted in sphalerites from well B1 and A4. The signals from fluid inclusions are marked by steep Na peaks. Zn concentrations in these fluid inclusions could not be measured due to overlapping signal from the host sphalerite. Fluid inclusions contain excess Ge, Tl and Pb compared to host sphalerite, which also contains these elements as structural substitutions
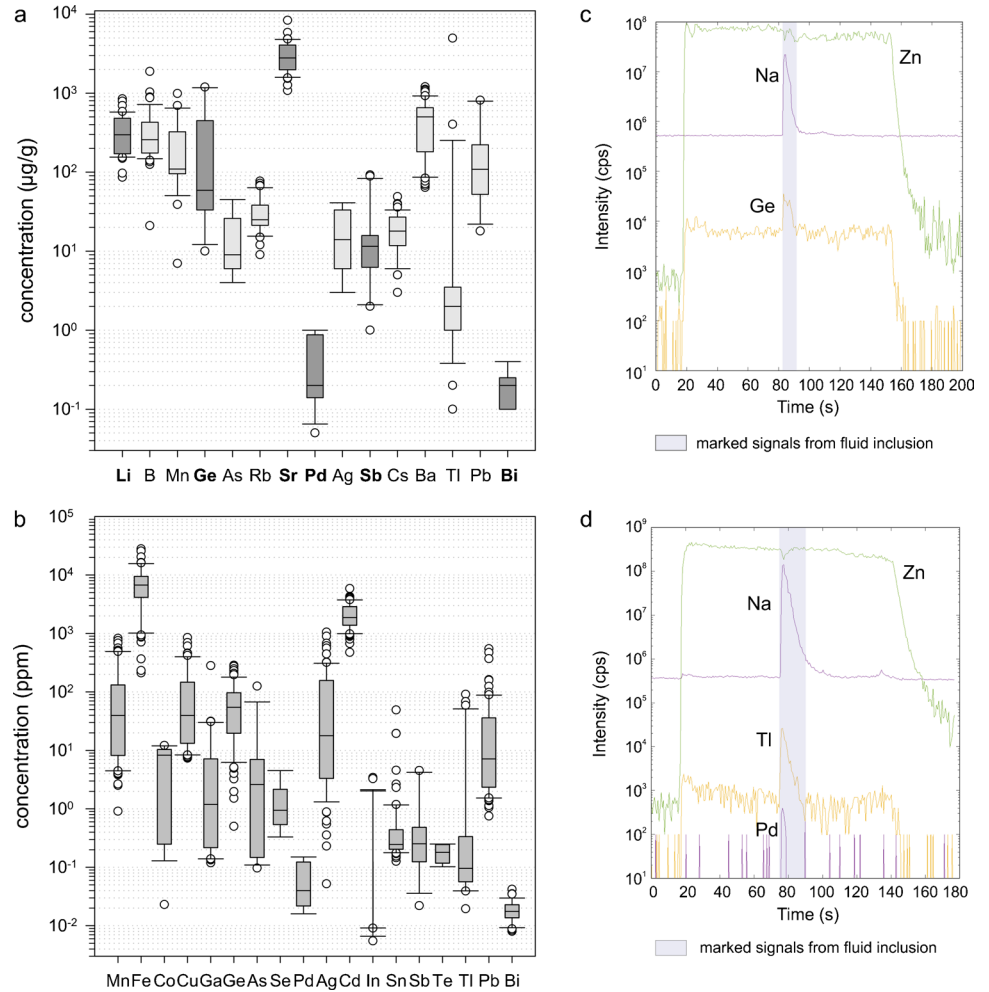

Fig. 8 Spider diagram showing median concentrations of trace elements in fracture-filling quartz-hosted fluid inclusions from Upper Carboniferous and Zechstein strata as well as sphalerite-hosted brine inclusions from Zechstein carbonate Ca2
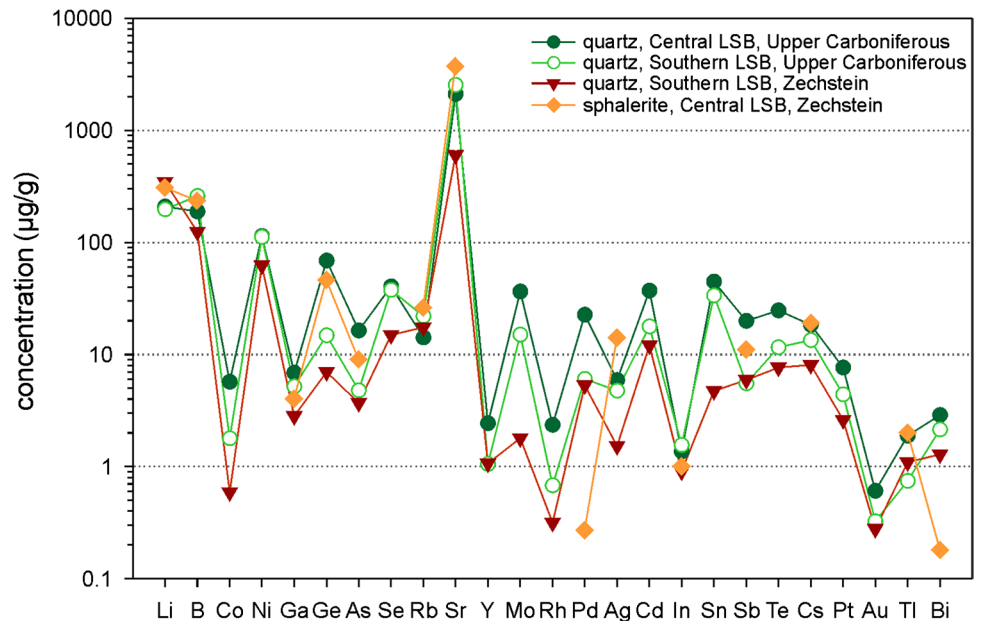
Table 1 Stable carbon isotope data of inclusion gases (CO_2, CH_4) hosted in sphalerite, quartz, fluorite and calcite-barite fracture-fillings in Zechstein and Upper Carboniferous strata from the central, western and southern parts of the Lower Saxony Basin

No.	Area	Sample No.	Stratigraphy	Mineral	$\delta^{13}C_{PDB}$ (CH_4), ‰	$\delta^{13}C_{PDB}$ (CO_2), ‰
1	central LSB	A3	Zechstein Ca2	sphalerite		–3.1
2	central LSB	A4	Zechstein Ca2	sphalerite		–9.0
3	central LSB	A1-39	Zechstein Ca2	sphalerite	–6.4	–1.4
4	central LSB	A1-40	Zechstein Ca2	sphalerite	–7.3	–1.7
5	southern LSB, Perm mine	IBB-1S	Zechstein Ca1	sphalerite	–26.0	–1.6
6	southern LSB, Perm mine	IBB-1Q	Zechstein Ca1	quartz	–24.7	
7	western LSB	B1-20_1	Zechstein Ca2	fluorite	–26.3	
8	western LSB	B1-20_2	Upper Carboniferous	calcite-barite	–24.6	
9	western LSB	B1-21	Upper Carboniferous	barite-calcite	–25.6	
10	western LSB	B1-19	Upper Carboniferous	barite-calcite	–26.1	

sphalerite from the Perm Mine, yielded a $\delta^{13}C_{CH4}$ value of −24.7‰, which is similar to inclusion gases from sphalerite (−26.0‰). The $\delta^{13}C_{CH4}$ values acquired from inclusion gases hosted in other fracture-filling minerals, i.e., fluorite, barite and calcite, in Ca2 and Upper Carboniferous strata in the western LSB, are very consistent and cover a range between −26.3 and −24.6‰.

Zechstein Ca2-hosted, zoned hydrothermal fracture-filling pyrites from the deep well PB-13, that was sunk close to the northern flank of the LSB (Fig. 1), were analyzed for *in situ* stable sulfur isotopic compositions. The $\delta^{34}S$ values range between −13.4 and −9.6‰, median: −12.2‰ (Fig. 9, Fig. 1 in Online Resource 1, Online Resource 4).

Noble gas isotopes

Noble gas isotope data of fluid inclusions from individual crushes of sphalerite separates are shown in Table 2. The analyzed inclusions are aqueous-dominated fluids of both primary, and pseudo-secondary and secondary origin, which may also contain trace amounts of CH_4, CO_2 and H_2S gases (Sośnicka and Lüders 2019). The highest $^3He/^4He$ ratios of 0.08–0.1 R_A are from dark sphalerites from the Perm Mine and the Ibbenbüren coal mining area in the southern LSB (Fig. 10a). In contrast, the zoned yellow-orange sphalerites from the deep well B1, sunk close to the western flank of the LSB, yielded the lowest $^3He/^4He$ ratios of 0.02–0.03 R_A (Fig. 10). The largest range of $^3He/^4He$ ratios (0.03–0.08 R_A) is shown by sphalerites from deep wells (A1, A3, A4) in the central LSB. The highest $^{40}Ar/^{36}Ar$ ratios are from brine inclusions hosted in meter-scale sphalerite ore zones from the deep well A1 (Fig. 10c). The isotopic ratios of the heavier noble gases (Ne, Xe) are very close to atmospheric values, within the error limits (Table 2, Online Resource 4). The results from the central part of the LSB show that relative abundances of Ne and Ar are similar to air, whereas Kr and Xe abundances are higher by fractionation

factors of ca. 1.5 and ca. 2–10, respectively (Fig. 2 in Online Resource 1). Data from the southern part of the LSB indicate the relative abundances of Ne, Ar and Kr are relatively close to the air abundances, while Xe abundances are higher by factor of ca. 2–5 (Fig. 2 in Online Resource 1).

Discussion

Major, trace, and critical elements in metalliferous fluids

Fluid inclusions hosted in fracture-filling minerals from each studied well and locality record unique metal concentration signatures (Figs. 5, 6, 8). In the central part of the LSB type I fluid inclusions, in individual samples from different wells show highly variable salinity and homogenization temperatures (Fig. 4), and based on these data three major fluid inclusion groups were distinguished: 1) group A moderate salinity halite-undersaturated (<26 wt% NaCl equiv.) and high-temperature, 2) group B high-salinity (~26 wt% NaCl equiv.) and low-temperature, and 3) group C very high-salinity (>> 26 wt% NaCl equiv.) and low-temperature (Fig. 4). In the southern LSB, only two groups (A, B) were observed (Fig. 4).

The fluid inclusion data from the Piesberg quarry, reported by Wüstefeld et al. (2017) are in very good agreement with our results from other sample sites in the Piesberg area. Minor sphalerite mineralization from the Piesberg quarry is associated with quartz II, which precipitated from high-salinity brines (17.7–21.6 wt% NaCl equiv.) with T_h values of 167–202°C during the Late Cretaceous inversion (Wüstefeld et al. 2017). Group B aqueous brines from other sites in the Piesberg area have similar T_h values (183–208°C) and slightly higher salinity values (22.6–27.5 wt% NaCl equiv.) and contain the highest metal concentrations
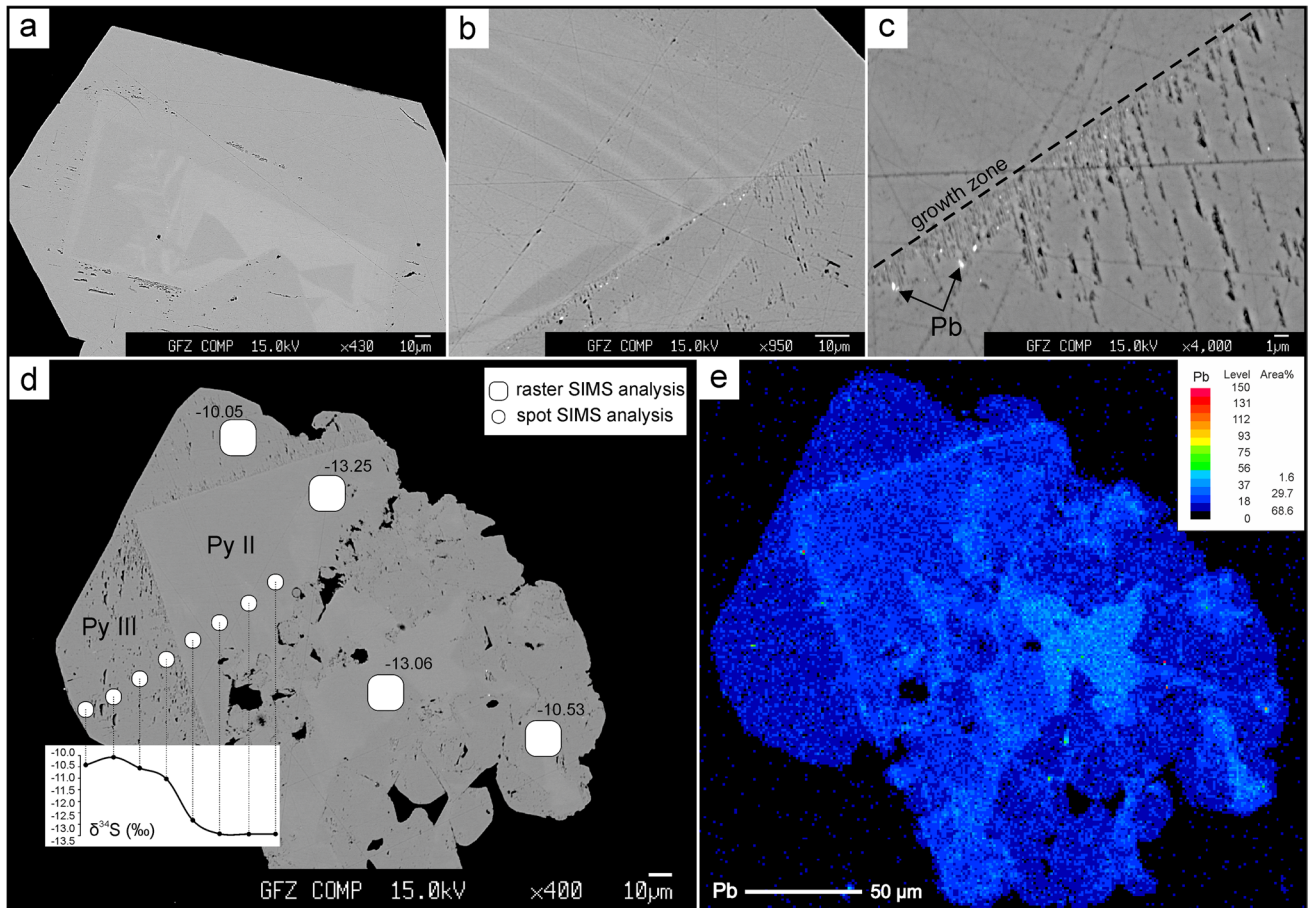
Fig. 9 Compositional zoning and *in situ* sulfur isotope data from hydrothermal pyrites (well PB-20). **a-b** BSE images of compositional zoning in pyrite II (Py II) as well as growth zones in the latest pyrite generation (Py III). **c** growth zone in Py III with inclusions of Pb-bearing solids (Pb). **d** BSE image with marked ion probe analytical points (white spots and squares), the inset illustrates a trend in δ^{34}S (‰ CDT) values along the spot line traversing two pyrite generations (Py II and III), **e** element map of Pb concentrations (cps) showing lack of systematic zoning from core to rim in Py II and III. Pyrite generation systematics is adapted from Sośnicka and Lüders (2020)

(Figs. 4–6). Thus, it is likely that their migration was also related to the Late Cretaceous inversion. Group B FIA's hosted in quartz, and sphalerite-hosted FIA's in the central LSB, clearly show similar/overlapping temperature and salinity data ranges (Fig. 4) suggesting that group B fluids are representative of ore fluids basin-wide. Groups B and C brine FIA's have the highest Zn and Pb concentrations in quartz from the Piesberg and the Perm Mine areas in the southern part of the LSB and in well D1 in the central part of the LSB, respectively (Figs. 5–6). The Zn concentrations in quartz-hosted type B fluid inclusions from sphalerite ore (Perm Mine) are comparable to those in group C inclusions hosted in fracture-filling quartz in well D1 (Figs. 5–6). These observations confirm that fluids B and C have a high metal endowment and would be the most suitable to become the ore-forming fluids. High salinities of these fluids (Fig. 4) indicate significant transport of Zn and Pb in the form of chloride complexes by either oxidized, acidic to near-neutral, or reduced acidic brines (Cooke et al. 2000).

The differing metal concentration trends, as shown by FIA's hosted in quartz fracture-fillings from the Upper Carboniferous (Figs. 5–6) can be ascribed to the different evolution during the structural re-organization and compartmentalization of the basin. The separate tectonic blocks would experience variable fluid residence times in the metal source regions and explain the lack of correlation between salinity and Zn concentrations in fluid inclusions on a basin scale (Figs. 5–6). However, differences in metal concentrations are clearly observable on a local scale, for example in samples from the Piesberg area or well D1 (Figs. 5–6), which suggests that the brines were probably stored in different isolated source rock compartments. Barium concentrations are elevated in fluids migrating through the Upper Carboniferous and drop by at least one order of magnitude in Zechstein units in the LSB (Figs. 5–6). Overall, relatively high Ba concentrations in fluids migrating through Upper Carboniferous strata suggest a more reducing fluid. The simultaneous transport of H_2S with Zn-Pb in such fluids can be excluded as the presence of considerable quantities of H_2S

Table 2 Results of noble gas analyses of fluid inclusions liberated by crushing of sphalerite separates from Zn-Pb ores in the central, western and southern parts of the Lower Saxony Basin. Concentrations are in cm³ STP per gram of rock. $R_A = 1.39 \times 10^{-6}$ is the atmospheric $^3He/^4He$ ratio. Error limits are 2σ

Sphalerite sample	^4He $10^{-8}\,cm^3/g$	^{20}Ne $10^{-12}\,cm^3/g$	^{40}Ar $10^{-8}\,cm^3/g$	$^{40}Ar*$ $10^{-8}\,cm^3/g$	$^3He/^4He$ R_A	$^{40}Ar*/^4He$	$^{20}Ne/^{22}Ne$	$^{21}Ne/^{22}Ne$	$^{40}Ar/^{36}Ar$	$^{38}Ar/^{36}Ar$	^{84}Kr $10^{-12}\,cm^3\,STP/g$	^{132}Xe $10^{-12}\,cm^3\,STP/g$
Lower Saxony Basin												
B1_4	125.4 ±6.3	1667 ±85	113.2 ±7.7	6.18 ±0.74	0.0225 ±0.0037	0.0493 ±0.0064	9.97 ±0.20	0.02942 ±0.00047	315.8 ±1.8	0.18799 ±0.00094	73.2 ±4.9	9.2 ±1.3
1.50106 g												
B1_6	221 ±11	2310 ±120	159 ±11	11.9 ±1.1	0.0261 ±0.0033	0.0540 ±0.0056	9.682 ±0.046	0.02945 ±0.00038	322.8 ±1.6	0.1880 ±0.0010	92.8 ±7.6	6.49 ±0.60
1.00346 g												
A1_40	1283 ±89	6270 ±350	437 ±30	144 ±10	0.0759 ±0.0094	0.112 ±0.011	10.055 ±0.045	0.03056 ±0.00030	444.9 ±2.4	0.18707 ±0.00095	201 ±13	17.3 ±1.3
0.80296 g												
IBB_1S	47.7 ±2.4	374 ±21	26.6 ±1.4	4.12 ±0.36	0.095 ±0.030	0.0864 ±0.0087	9.716 ±0.089	0.03068 ±0.00089	353.3 ±4.6	0.1883 ±0.0015	18.2 ±1.2	3.03 ±0.37
0.19976 g												
A4_83	395 ±20	994 ±56	68.7 ±3.4	12.99 ±0.70	0.0432 ±0.0052	0.0329 ±0.0024	9.789 ±0.063	0.02996 ±0.00061	368.2 ±1.8	0.1888 ±0.0011	59.0 ±3.6	18.9 ±1.5
0.49976 g												
PERM_5+6	38.0 ±1.9	777 ±44	46.7 ±2.3	3.03 ±0.29	0.077 ±0.020	0.0798 ±0.0086	9.810 ±0.053	0.02949 ±0.00091	319.3 ±1.8	0.1887 ±0.0011	31.7 ±1.9	4.02 ±0.85
0.50100 g												
A4_84	318 ±16	6020 ±340	412 ±28	7.9 ±2.4	0.0520 ±0.0067	0.0249 ±0.0076	9.868 ±0.052	0.02929 ±0.00035	304.4 ±1.8	0.1890 ±0.0010	391 ±25	42.3 ±6.9
0.49878 g												
A3 dark brown	290 ±15	1750 ±98	107.4 ±5.4	4.66 ±0.55	0.0330 ±0.0049	0.0161 ±0.0021	9.820 ±0.055	0.02943 ±0.00062	312.1 ±1.5	0.1897 ±0.0010	83.2 ±5.1	17.0 ±1.5
0.49942 g												
A3 yellow	242 ±12	1105 ±81	66.0 ±3.3	4.31 ±0.39	0.0328 ±0.0045	0.0178 ±0.0018	9.832 ±0.091	0.02948 ±0.00065	319.4 ±1.7	0.18850 ±0.00097	43.9 ±3.6	5.98 ±0.55
0.48584 g												
Harz Mountains												
Lautenthal	137.8 ±6.9	279 ±21	20.2 ±1.0	4.38 ±0.27	0.0795 ±0.0097	0.0318 ±0.0025	9.849 ±0.099	0.0300 ±0.0014	381.2 ±3.9	0.1869 ±0.0013	11.53 ±0.96	1.79 ±0.23
0.50506 g												
Atmosphere					*1*		*9.8*	*0.029*	*298.56*	*0.1885*		

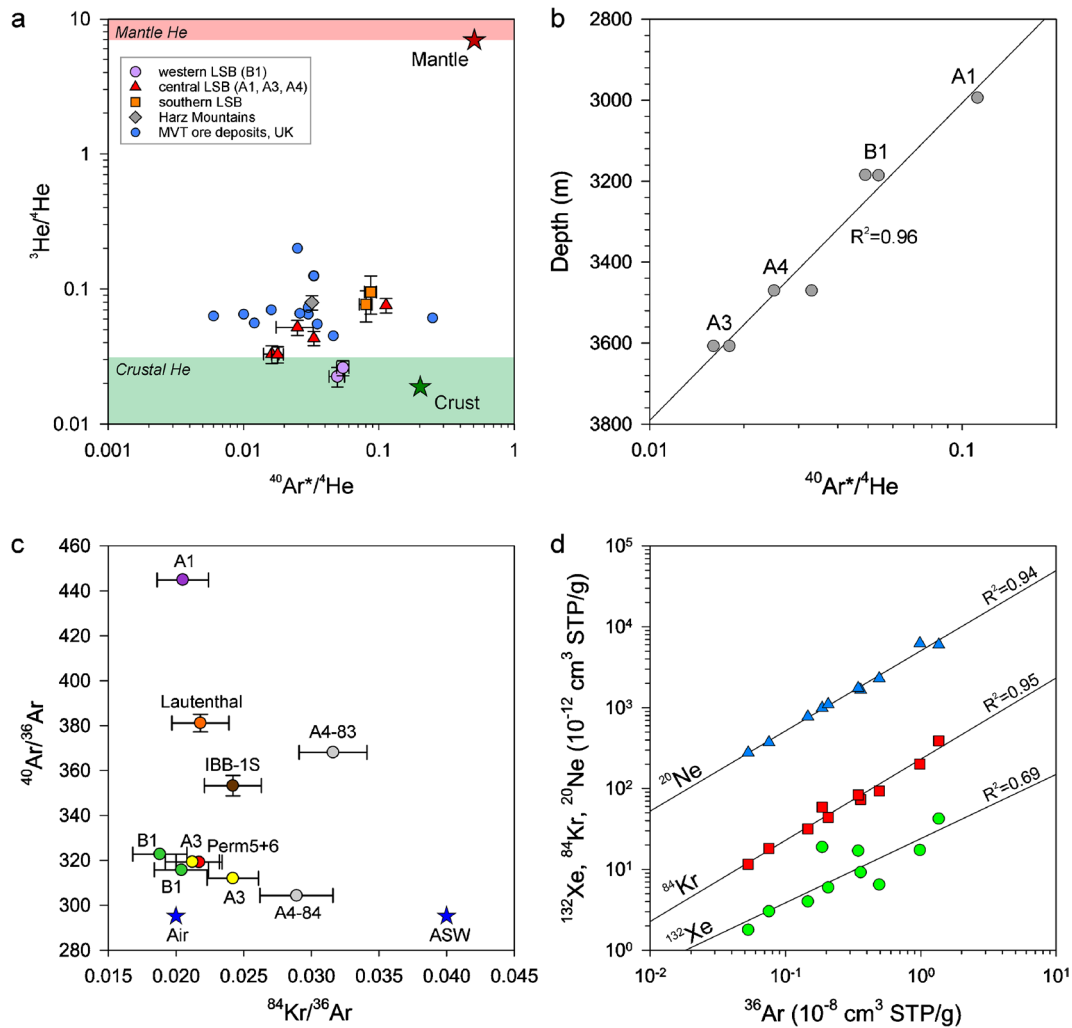**Fig. 10** Noble gas isotope data from the Lower Saxony Basin and Harz Mountains (Lautenthal Zn-Pb deposit). **a** Diagram of ^{3}He/^{4}He versus ^{40}Ar*/^{4}He for fluid inclusions hosted in sphalerites from different parts of the LSB (southern: Ibbenbüren and Perm Mine, central: deep wells A1, A3 and A4, and western: deep well B1) and hydrothermal sphalerite from the Harz Mountains (Lautenthal Zn-Pb deposit). Estimates of the ^{40}Ar*/^{4}He and ^{3}He/^{4}He ratios for the mantle and crust are shown as star symbols. Crustal excess ^{40}Ar* is given by the equation: ^{40}Ar* = ^{40}Ar$_{total}$ × [1-(^{40}Ar/^{36}Ar)$_{air}$/(^{40}Ar/^{36}Ar)$_{sample}$] (Ballentine et al. 2002). Data from quartz and fluorite from the North Pennine MVT orefield, UK (Stuart and Turner 1992; Ballentine and Burnard 2002) is included for comparison. **b** sampling depth vs. ^{40}Ar*/^{4}He ratios diagram, inverse correlation is observed. **c** ^{40}Ar/^{36}Ar vs. ^{84}Kr/^{36}Ar diagram, data points located closest to the air value show the highest contamination with modern atmosphere, whereas data points with the highest ^{40}Ar/^{36}Ar ratios are ascribed to the longest crustal residence. **d** ^{36}Ar abundances vs. ^{132}Xe, ^{84}Kr and ^{20}Ne, correlation between ^{132}Xe and ^{36}Ar is not as strong as for ^{84}Kr or ^{20}Ne. Where error bars are not shown in **a** and **b** they are equal to or smaller than the symbol size

would have prevented the transport of high amounts of Zn and Pb resulting in sulfide precipitation. This is consistent with the absence of detectable H$_2$S in the vapor bubbles of metal-rich fluid inclusions and associated gas inclusions, hosted in quartz fracture-fillings from the Upper Carboniferous as well as Zechstein Ca1 strata, as constrained by Laser Raman spectroscopy. The decrease of Ba content in fluid inclusions in ore and gangue minerals, hosted by Zechstein Ca2 reservoir rocks (Figs. 5–6), is likely due to mixing with Zechstein-derived fluids or barite precipitation in fractures at the top of the Upper Carboniferous.

Fluid inclusion data from quartz fracture-fillings hosted by Upper Carboniferous strata in the LSB show very high Zn and Pb concentrations, reaching up to thousands of μg g^{-1}, and which are comparable with fluid inclusion data from fracture-filling minerals in Rotliegend and Carboniferous strata of the North-East German Basin (Zn: up to 8470 μg g^{-1}, Pb: up to 2257 μg g^{-1}, Lüders et al., 2005) (Fig. 11). These fluids are significantly more enriched in metals relative to modern basinal brines (McCaffrey et al. 1987), suggesting that efficient metal enrichment processes were operating at depth. This also shows that metal contents

Fig. 11 Zn and Pb concentrations in fluid inclusions hosted in fracture-filling quartz from Upper Carboniferous and Zechstein strata in the Lower Saxony Basin. Fluid inclusion data from fracture-filling calcite hosted by Rotliegend sandstones and quartz hosted by Namurian (Carboniferous) sandstones in the North-East German Basin-NEGB (Lüders et al. 2005) as well as data from quartz-hosted fluid inclusions of world-class Zn-Pb MVT ore districts in the U.S.A. (Stoffell et al. 2008) are shown for comparison. Compositions of modern basinal brines are after Carpenter et al. (1974)
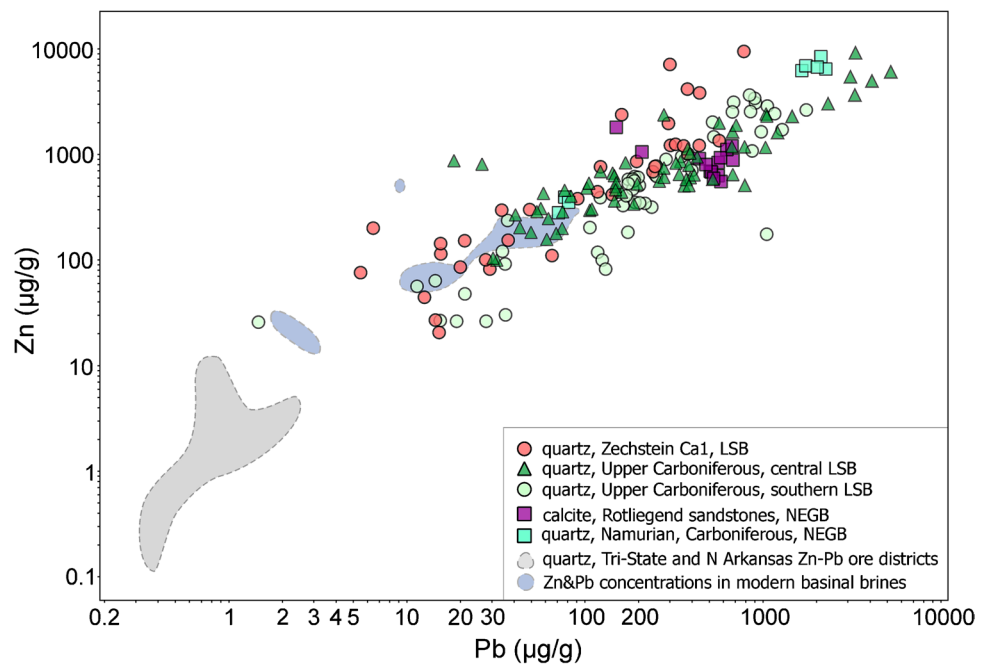
of fluids from the LSB are much higher compared to fluids reported from giant MVT Zn-Pb districts in Northern America (Fig. 11).

Sphalerite-hosted fluid inclusions from deep-seated mineralization in the central part of the LSB contain elevated concentrations of the trace elements: Li, B, Mn, Rb, Sr, Cs, Ba, Tl, Ag, As and Pb (Figs. 7a, 7d, 8). In addition, the enrichment of certain critical metals such as Ge to concentrations of thousands of µg g^{-1} and lesser amounts for In, Pd, Sb and Bi are observed (Figs. 7a, 7c-d, 8). Mobile elements such as Tl and Sb tend to be concentrated in the fluid and their enrichment is indicative of intensive fluid-rock interactions (Jochum and Verma 1996). Although Sb is rarely observed in the sphalerite matrix (Cook et al. 2009), our data imply that the studied sphalerites precipitated from a fluid containing 1–92 µg g^{-1} Sb (Table 1 in Online Resource 1). Thallium is a common substitution in the sphalerite structure, and this is consistent with its presence in the sphalerite-hosted fluid inclusions (Fig. 7a). Palladium is the most mobile element within the PGE group, however, aqueous speciation and mobility of this metal in low-temperature hydrothermal systems remains controversial, according to recent experimental studies (Tagirov et al. 2013; Mei et al. 2015). It has been shown that $PdCl_3^{2-}$ and $PdCl_4^{2-}$ complexes are not stable under low-temperature hydrothermal conditions (<350°C) and are transported by sulfur-poor, acidic, oxidized fluids, whereas neutral-alkaline, reduced fluids carry Pd as $Pd(HS)_4^{2-}$ (Tagirov et al. 2013; Bazarkina et al. 2014; Mei et al. 2015). This is partly in agreement with our results from high-salinity fluid inclusions in fracture-filling quartz, as they do not contain detectable sulfur, however,

they represent a lower temperature fluid (<250°C). The Pd concentrations in these inclusions are at least one order of magnitude higher compared to sphalerite-hosted fluid inclusions (Fig. 8), which suggests that this metal was sourced from the siliciclastic strata underlying the Zechstein evaporitic sequence. Anomalous concentrations of noble metals such as Pd and Pt were, for example, found in the ore-bearing shale of the Polish Kupferschiefer-type Cu-Ag deposits, and could be released by alteration of organic matter by catalytic auto-oxidation and desulfurization processes (Kucha 1982; Kucha and Przybyłowicz 1999; Piestrzyński et al. 2002). Therefore, the sphalerite-forming fluid must have interacted (at least partly) with organic-rich rocks (coals or shales) to acquire such a diverse metal budget. Germanium is depleted in evaporitic sequences, thus Zechstein carbonates are an unlikely source of this metal. However, coal seams are enriched in Ge, with concentrations reaching up to a few thousands of ppm, due to adsorption on organo-complexes such as humic acids (Höll et al. 2007). The similar median Ge concentrations in fluid inclusions hosted in sphalerites from Zechstein Ca2 and quartz fracture-fillings from the Upper Carboniferous in the central LSB, imply that Ge was also scavenged by the ore-forming fluids from Westphalian coals and Silurian/Namurian/Westphalian coaly shales (Fig. 8). Median trace element concentrations in fluid inclusions hosted in fracture-filling quartz from the Upper Carboniferous in the central and southern LSB show very similar patterns (Fig. 8). Interestingly, the median concentrations of the sphalerite-hosted fluid inclusions are lower for most elements, i.e., Li, B, Ga, Ge, As, Rb, Sr, In, Sb, Cs and Tl, than in the quartz-hosted fluid inclusions (Fig. 8). The

geochemical signature from sphalerite-hosted fluid inclusions is distinct only in case of three elements, i.e., Pd, Ag and Bi (Fig. 8), which may be related to mixing (Sośnicka and Lüders 2019) or simultaneous precipitation of other sulfides, e.g., galena, and resulting element partitioning between the ore mineral phases.

Fluid inclusions hosted in sphalerite have a slightly different trace metal budget compared to the host mineral (Fig. 7a–b). For example, Cu, Fe, Cd, and Sn were not detected in fluid inclusions, but are present in the sphalerite crystals (Knorsch et al. 2020). This suggests that as they partitioned into the sphalerite structure, the ore fluid was depleted in these elements and/or their concentrations in fluid inclusions were too low to overcome that from the sphalerite crystals. The latter is highly probable for elements such as Fe and Cd, which are abundant in sphalerite (Fig. 7b). Although Sn was not detected in sphalerite-hosted fluid inclusions, it is present in sphalerite (Fig. 7b) as well as in quartz-hosted fluid inclusions from Zechstein Ca1 and Upper Carboniferous strata (Fig. 8). Sn has rarely been reported in sphalerites (Cook et al. 2009) and significant quantities of this metal can be transported solely in reduced fluids (Cooke et al. 2000). The sphalerite-hosted fluid inclusions show overall high concentrations of Ge, Tl and Mn (up to 1194 µg g^{-1}, 4953 µg g^{-1}, 986 µg g^{-1} respectively, Figs. 7a, c–d, 8) compared to their host sphalerites, which contain up to 285 ppm Ge, 91 ppm Tl, and 826 ppm Mn (Knorsch et al. 2020). Ag was incorporated into the sphalerite structure with concentrations up to 1054 ppm (Knorsch et al. 2020), but are lower in the fluid inclusions (3–41 µg g^{-1}) representing the sphalerite-forming fluid (Figs. 7a–b, 8).

Fluid source regions and reservoirs

The analyses of noble gas isotope compositions in sphalerite-hosted fluid inclusions from Zn-Pb ore deposits in the LSB allow the discrimination of potential fluid reservoirs (Fig. 10a). The data plotted in the ^{3}He/^{4}He vs. ^{40}Ar*/^{4}He diagram (Fig. 10a), where ^{40}Ar* is the air-corrected (radiogenic) fraction of ^{40}Ar, point towards a significant contribution of crustal reservoirs as sources of noble gases in the analyzed fluid inclusions. The contribution of atmospheric ^{4}He is negligible due to low abundances in the atmosphere (Ballentine et al. 2002) and large (^{4}He/^{20}Ne)$_{sample}$ abundance ratios, ranging between 490 and 4900 (av. 1880), which are 3–4 orders of magnitude above the air-saturated water (ASW) value of ca. 0.27. Furthermore, the calculation of the crustal contribution ^{4}He$_{crust}$, following Ballentine et al. (2002) and assuming ^{3}He/^{4}He$_{crust}$ of ~1 × 10^{-8} and ^{3}He/^{4}He$_{mantle}$ of 854 × 10^{-8} (subcontinental lithospheric mantle), reveals that ^{4}He trapped in fluid inclusions (38–1283 × 10^{-8} cm^3 STP/g of rock), has been produced in the crust without any significant contribution of an additional mantle component. The measured ^{3}He/^{4}He range of 0.02–0.1 R$_A$ (Fig. 10a, Table 2) in the brine inclusions is too low ($\leq$0.1 R$_A$) to unequivocally indicate ^{3}He contribution from mantle degassing in a continental setting. The LA-ICP-MS analyses have shown that brine inclusions hosted in sphalerites contain considerable quantities of Li (86–846 µg g^{-1}, median: 297 µg g^{-1}, Figs. 7a, 8). Therefore, it is more likely that thermal neutron activation of ^{6}Li was responsible for the production of additional ^{3}He (Mamyrin and Tolstikhin 1984) and gave rise to the slightly elevated ^{3}He/^{4}He ratios of 0.02–0.1 R$_A$. Alternatively, counterbalancing this is the decay of ^{40}K, that is also present in the brine inclusions (827–25369 µg g^{-1}, median: 5710 µg g^{-1}), and which likely contributed to production of additional crustal ^{40}Ar* in fluid inclusions. It has been previously shown in noble gas studies of sulfide minerals, including sphalerites, that post-entrapment production of ^{3}He and ^{4}He is minor relative to the values measured (Ballentine et al. 2002). If minor post-entrapment production is assumed in this study, then ^{3}He must have been produced in the original Li-rich source rock or a minor mantle contribution has to be considered. The presence of cosmogenic He can be excluded as sampling depths exceed 2.9–3.5 km (Sośnicka and Lüders 2019).

Sphalerite-hosted fluid inclusions from the Perm Mine and the deep well A1 show the highest ^{3}He/^{4}He ratios approaching 0.1R$_A$ (Fig. 10a, Table 2), which are at the lower limit of data from the Bramsche area (Fig. 1) that is known for the presence of overmature organic matter in the Paleozoic strata (Lüders et al. 2021). The most radiogenic compositions (^{3}He/^{4}He = 0.02 R$_A$), in fluid inclusions from deep wells in the western LSB, fall within the crustal He field, i.e., they agree with the crustal production ratio of 0.01–0.05 R$_A$ (Fig. 10a). The radiogenic ^{4}He is derived from radioactive decay of U and Th-rich mineral phases and can be released and incorporated into the fluids during crustal degassing (Ballentine et al. 2002). The Zn-Pb ore, in the western LSB, directly overlies Carboniferous strata composed of hydrothermally altered muscovite-rich sandstones, coaly mudstones, and coals, which are excellent sources of K-rich phases (muscovite, biotite, feldspar) as well as accessory U-bearing phases (monazite, uraninite). Hydrothermal alteration of the latter minerals, present in the host rocks, most likely resulted in a release of radiogenic ^{40}Ar* and ^{4}He into the ore-forming fluids by thermal diffusion or chemical dissolution (Stuart and Turner 1992). All ^{40}Ar*/^{4}He values (0.02–0.11) from sphalerite-hosted fluid inclusions are lower than the average crustal production ratio (^{40}Ar*/^{4}He = 0.2, Stuart et al., 1995). The spread of ^{40}Ar*/^{4}He ratios between the wells and areas in the LSB (Fig. 10a) is caused by fractionation of Ar from He, and can be ascribed to different crustal levels and thermal conditions in the source regions. There is an inverse correlation (R^2 = 0.96) between the sampling depth and ^{40}Ar*/^{4}He ratios (wells A1, A3, A4,

B1), which decrease with increasing depth (Fig. 10b). This is not consistent with lower closure temperatures for radiogenic ^{4}He compared to ^{40}Ar, that should consequently result in lower ^{40}Ar*/^{4}He ratios at shallower crustal levels (Lippolt and Weigel 1988). Furthermore, there is no correlation between sampling depth and ^{4}He abundances. This suggests that factors other than geothermal gradient, e.g., widespread mobilization of hot hydrothermal fluids and sourcing from more than one lithology, controlled diffusion of crustal ^{4}He and ^{40}Ar into the fluids, in the over-pressured source regions in the LSB. It has been anticipated that semi- to non-permeable rocks, e.g., shales, mudstones, coals or salts, in sedimentary basins, have a good capacity to accumulate noble gases and thus significantly hinder their diffusion towards shallower crustal levels (Pinti and Marty 1998). In contrast, more porous rocks such as sandstones allow relatively high He fluxes (Ballentine et al. 2002). As the studied Zn-Pb ore zones and deposits are situated in the evaporitic over-pressured basin (Sośnicka and Lüders 2019), the noble gas transport occurred by advection through structural discontinuities during protracted tectonic activity. The structurally controlled migration of ore-forming fluids led to the interaction with brines stored in differently pressured rock compartments and flushing out helium and other noble gases from different rock types resulted in a diverse inventory of radiogenic and atmosphere-derived noble gases (Fig. 10). The highest ^{4}He concentrations in fluid inclusions, hosted in sphalerites from deep well A1 (1283±89 × 10^{-8} cm^3 STP/g, respectively) suggest the highest fluid residence times and that the noble gas exchange with deeply covered crystalline basement rocks occurred through deep-reaching thrust zones which constitute the northern borders of the LSB (Fig. 1). The crustal ^{40}Ar* abundances in the ore fluids from the LSB range between 3.0 and 13 × 10^{-8} cm^3 STP/g of rock, with one exception. The highest radiogenic ^{40}Ar* = 144 × 10^{-8} cm^3 STP/g and the highest ^{40}Ar/^{36}Ar ratio of 444.9 (Fig. 10c, Table 2), and ^{40}Ar*/^{4}He ratio of 0.112, which is the closest to the crustal production ratio of ~0.2, were observed in sphalerite-hosted brine inclusions from deep well A1 in the central LSB (Fig. 10a). Moreover, a slight enrichment in nucleogenic ^{21}Ne* (^{21}Ne/^{22}Ne = 0.03056±0.00030) compared to air (Table 2) is also observed in the inclusion fluids. The significant enrichment in ^{4}He, ^{40}Ar*, and ^{21}Ne* in the ore fluid, which was responsible for precipitation of the thickest, meter-scale ore zones in deep well A1, pinpoints the highest degree of fluid interaction with the underlying strata and crystalline basement in the LSB. The ^{21}Ne* enrichment can also be attributed to the presence of minor quantities of isotopically light CH$_4$ (Table 1), which carries the noble gas signature of hydrocarbon source rocks, i.e., Carboniferous coals and coaly shales. Previous noble gas studies of hydrocarbon reservoirs have shown that natural CH$_4$-dominated gases are enriched in nucleogenic

^{21}Ne* (Torgersen and Kennedy 1999; Kennedy et al. 2002). High crustal ^{40}Ar* abundances in fluid inclusions also point towards the longest crustal residence time of the ore fluids, which may be attributed to fluid trapping in isolated aquifer compartments or a release from over-pressured, tectonically induced floater blocks at the flanks of the LSB.

The close-to-atmospheric isotopic ratios of the heavy noble gases Ne and Xe, from sphalerite-hosted brine inclusions, indicate equilibration with paleo-atmosphere or dissolution in air-saturated water (ASW) (Table 2, Online Resource 4). The ^{84}Kr/^{36}Ar element ratios (0.019–0.032), in a range between air and ASW values (Fig. 10c), also show that these noble gases are of atmospheric origin and were derived from air-saturated seawater, formation or meteoric water. The fractionation of heavy noble gases (Ne, Kr, Xe) was assessed relative to ^{36}Ar and air (Fig. 2 in Online Resource 1). The dissolution equilibrium curves (Fig. 2 in Online Resource 1) were plotted for air-saturated water at temperatures of 0°C and 50°C at salinity of 25 wt% NaCl equiv. as well as for 100°C, 250°C, and 330°C at zero salinity due to lack of experimental data for high-salinity fluids at high temperatures (≥100°C). Fractionation factors of Kr cluster tightly near the isotopic equilibrium curve for 250°C for all wells and areas except well A4, for which they match the dissolution equilibrium curve for 100°C more closely (Fig. 2 in Online Resource 1). Microthermometry data from fluid inclusions hosted in sphalerites of massive as well as vein-type ores, in the western and central LSB, show temperatures of 125–171°C (well B) and 153–207°C (wells: A3, A4), respectively (Sośnicka and Lüders 2019). A similar temperature range of 145–196°C was reported from Zn-rich inclusions hosted in quartz intergrown with sphalerite ore from the Perm Mine in the southern LSB (Fig. 5). Temperatures of sphalerite precipitation were influenced by fluid mixing (Sośnicka and Lüders 2019) and are consistent with the equilibrium dissolution of atmospheric noble gases (Kr) into the ascending metal-rich fluid end-member at ca. 250°C prior to mixing. Such temperatures were achieved by fluids penetrating the Upper Carboniferous strata as shown by microthermometry (Figs. 4, 5). A lower dissolution temperature of 100°C, matching the Kr abundance in sphalerite-hosted fluid inclusions from well A4 (Fig. 2 in Online Resource 1), suggests that isotopic equilibrium was not reached, perhaps due to the presence of isotopically light carbon dioxide in the inclusions (Table 1). The Ne and Xe abundances do not show any obvious pattern in relation to the dissolution equilibrium curves (Fig. 2 in Online Resource 1). The high salinities of sphalerite-hosted fluid inclusions (21–32 wt% NaCl equiv., Sośnicka and Lüders, 2019) may be responsible for an increase of Ne/Ar ratios at higher temperatures ≥100°C (Desanois et al. 2019) and consequently higher

Ne abundances relative to the plotted fractionation curves (Fig. 2 in Online Resource 1). The excess of xenon in the sphalerite-forming fluids in the central LSB (Fig. 2 in Online Resource 1) can be attributed to more intense interaction with host rocks, that were enriched in Xe by preferential adsorption on mineral surfaces (Niedermann and Eugster 1992). Although ^{132}Xe and ^{36}Ar abundances show a positive correlation ($R^2 = 0.69$), it is not as significant as between ^{36}Ar and other non-radiogenic noble gases, i.e., Ne and Kr ($R^2 = 0.9$) (Fig. 10d). Alternatively, Xe and Kr enrichments can be also associated with traces of hydrocarbon gases (Torgersen and Kennedy 1999), which are present in the analyzed fluid inclusions (Table 1). A study of hydrocarbon gas-free fluid inclusions has shown Xe enrichments of up to a factor of 3 (Desanois et al. 2019), whereas in this study Xe enrichment is much higher, up to a fractionation factor of 10 (Fig. 2 in Online Resource 1). Sphalerite-hosted fluid inclusions from deep wells, which showed the highest enrichment in Xe by factor of ca. 4–10 (Fig. 2a in Online Resource 1), also contain traces of isotopically light TSR-derived CO_2 (Table 1). On the other hand, samples with CH_4 traces in fluid inclusions (Table 1) show Xe excesses by a factor of ca. 4–5 (Fig. 2b in Online Resource 1). It has been shown that carbon can be an effective carrier of Kr and Xe excess and that such enrichments are common in *in situ* hydrocarbon-generating source rocks (Torgersen and Kennedy 1999), e.g., coals or carbonaceous shales. Therefore, Xe enrichment is very likely a preserved source rock signature and confirms that Zechstein Ca2 reservoir sour gases in the LSB played a role in the genesis of the deep-seated Zn-Pb ores.

Overall in the context of noble gas data, prevalent radiogenic and atmospheric contributions imply that the Zn-Pb ore-forming fluids in the LSB represent heated brines, modified to variable degrees by interactions with stored formational brines as well as crustal rocks, including crystalline basement and a coal-bearing sedimentary sequence. The range of ^{3}He/^{4}He ratios of sphalerite-hosted brine inclusions in the LSB (0.02–0.1R_A) is similar to that of fluid inclusions hosted in fracture-filling minerals (quartz, fluorite, calcite) from: Zechstein Ca2 reservoirs, Carboniferous blocks in the Bramsche area, and deep Devonian strata in the LSB (Lüders et al. 2021). The noble gas isotope signature from fluid inclusions hosted in hydrothermal sphalerite from the Lautenthal deposit in the Harz Mountains (SE of the LSB), is similar to data from Zn-Pb ores in the LSB, suggesting a crustal contribution and a low probability of additional input from mantle degassing (Fig. 10a). The ^{40}Ar/^{36}Ar ratios range of 304–445 (Table 2), acquired from sphalerite-hosted inclusions in the LSB and the Harz Mountains, is similar to the isotope ratios of ore fluids (^{40}Ar/^{36}Ar = 320–420) from the world-class Viburnum Trend and Tri-State MVT Zn-Pb ore districts (Kendrick et al. 2002a). Fluid inclusions

in early sphalerite from the Viburnum Trend district yielded ^{40}Ar/^{36}Ar = 308±7 (Kendrick et al. 2002a), which is close to the lower limit of the isotope range from this study (Table 2). The ^{40}Ar/^{36}Ar ratios of 327–519 acquired from the F-rich MVT ore fluids, which deposited quartz and fluorite in the North Pennines orefield, UK (Stuart and Turner 1992), are also consistent with data from the ore brines of the LSB (Fig. 10a). The low ^{3}He/^{4}He ratios (0.02–0.1R_A), measured in sphalerite-hosted ore brines (Fig. 10a), are consistent with data from other MVT ore fluids in settings such as North Pennines orefield, UK (0.06–0.1R_A, Fig. 10a, Stuart and Turner, 1992), or South Pennine orefield, UK (0.02–0.07R_A, Kendrick et al., 2002b). This precludes dissolution of any significant amounts of mantle-derived helium into the ore fluids, which are therefore ascribed to a predominantly crustal origin. This implies that the ore brines precipitating sphalerite in the LSB and MVT ore fluids share a set of common characteristics with respect to noble gases and thus are likely a representative of such fluids. This is consistent with the MVT ore genetic model proposed for the deep-seated Zn-Pb ores in the LSB (Sośnicka and Lüders 2019).

Origin of ore-forming fluids

Halogen ratios of fluid inclusions hosted in quartz from Upper Carboniferous and Zechstein Ca1 strata provide constraints on the origin of the ore-forming fluids and their salinity. Analyses of halogens (Cl, Br) show that fluid inclusions, with similar salinity and temperature (Fig. 4), may have gained salinity by different processes (Fig. 12a). Quartz-hosted, group B type I fluid inclusions from samples D3-73 and A2-40, with similar salinities (Figs. 4b, 6), plot on opposite sides of the seawater value (SW) in the Na/Br vs. Cl/Br diagram (Fig. 12a). The Cl/Br ratios of brine inclusions from sample D3-73 are above the seawater value (SW), with one exception, and indicate that the salinity was derived by halite dissolution. These inclusions show distinctly higher Fe contents compared to group B inclusions from other deep wells in the central LSB (Fig. 6). The precipitation of the fracture-filling quartz from sample D3-73 was likely related to a normal fault, acting as a conduit that allowed fluid migration close to the flank of a nearby salt pillow (Fig. 1), and thus acquisition of salinity by salt dissolution. In contrast, Cl/Br ratios below the seawater value, and following the seawater evaporation trajectory, are characteristic for brine inclusions from sample A2-40 (Fig. 12a), and suggest salinity acquisition from seawater, evaporated past halite saturation. Similar halogen ratios of Upper Carboniferous formation waters and group B brine inclusions imply that the fracture-filling quartz from well A2-40 precipitated from a fluid that represents evaporated pre-Zechstein meteoric fluids, seeping into the siliciclastic Upper Carboniferous strata. Quartz-hosted group A fluid inclusions (Fig. 4b) from

Fig. 12 Cl/Br and Na/Br molar ratios of individual fluid inclusions hosted in quartz. **a** Data from group A, B and C, type I fluid inclusions, hosted in fracture-filling quartz, Upper Carboniferous, central LSB. **b** Data from group A and B, type I fluid inclusions, hosted in fracture-filling quartz, from uplifted Upper Carboniferous blocks and group B brine inclusions from Zechstein Ca1-hosted quartz (Alstedde/Schafberg) and from quartz intergrown with sphalerite ore from the Perm Mine, southern LSB. Fluid inclusion crush leach data are from Piesberg (quartz I and II, Upper Carboniferous) and Alstedde/Schafberg near Ibbenbüren (Zechstein Ca1). Compositions of formation waters from the Upper Carboniferous in the Lower Saxony Basin, from Lüders et al. (2010), are included for comparison. The halogen data clearly illustrates that fluids, although of similar salinities, gained their salinity by different processes. The seawater evaporation trajectory, which is marked by a dotted line, and points of first appearance of evaporite minerals, are from Viets et al. (1996). Saturation of the first appearing evaporite minerals occurs at higher Cl/Br and Na/Br ratios (Viets et al. 1996). The dashed line represents ratios of Na:Cl = 1
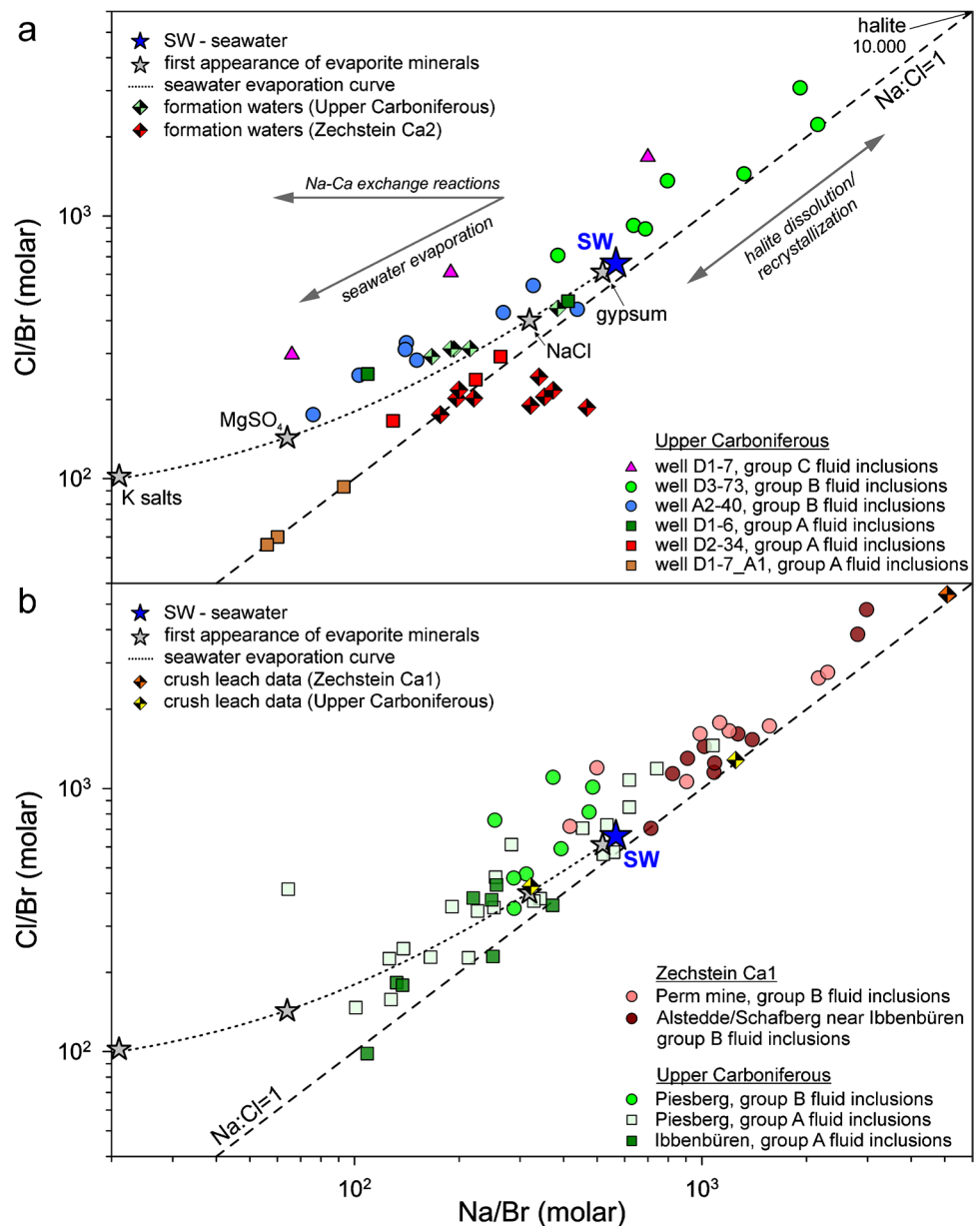
all samples collected from deep wells in the central LSB have halogen ratios pointing towards evaporation processes (Fig. 12a). Halogen data of group A fluid inclusions hosted by the fracture-filling quartz from well D2-34 are similar to those of present-day, sulfur-bearing formation waters in Zechstein Ca2 reservoirs (Figs. 12a, 13a, Online Resource 4). The origin of the highest salinity group C fluid inclusions (Fig. 4b) is more ambiguous as the data plot on both sides of the SW value (Fig. 12a). The most likely scenario is that the salinity of the group C brines resulted from mixing of seawater evaporated brines and halite dissolution brines.

All group B and the majority of group A fluid inclusions hosted by fracture-filling quartz from the Upper Carboniferous in the southern LSB plot along or close to the seawater evaporation trajectory; therefore, these fluid inclusions have solely or predominantly a halite-saturated seawater component (Fig. 12b). In contrast, the fluid inclusion data from Zechstein Ca1 shows Cl/Br ratios higher than the seawater value suggesting halite dissolution as a major source of salinity (Fig. 12b). The origin of the group A fluid, precipitating quartz fracture-filling in the Upper Carboniferous Piesberg block, is unclear as some Cl/Br ratios are higher than the SW value (Fig. 12b), suggesting that halite dissolution also contributed to the fluid salinity. This assumption is specifically valid for the data from brine inclusions hosted in quartz intergrown with sphalerite ore (Fig. 3e–f) from the Perm Mine, as they may represent a fluid which resulted from mixing of two fluid end-members: ascending metalliferous brine

Fig. 13 Cl/Br and Na/K molar ratios of individual fluid inclusions hosted in quartz.
a Data from group A, B and C, type I fluid inclusions hosted in fracture-filling quartz, Upper Carboniferous, central LSB.
b Data from group A and B, type I fluid inclusions hosted in fracture-filling quartz from uplifted Upper Carboniferous blocks and group B, brine inclusions from Zechstein Ca1-hosted quartz (Alstedde/Schafberg) and from quartz intergrown with Zn-Pb ore from the Perm Mine, southern LSB. Fluid inclusion crush leach data are from Piesberg (quartz I and II, Upper Carboniferous) and Alstedde/Schafberg near Ibbenbüren (Zechstein Ca1). Compositions of formation waters from the Upper Carboniferous in the LSB are from Lüders et al. (2010)
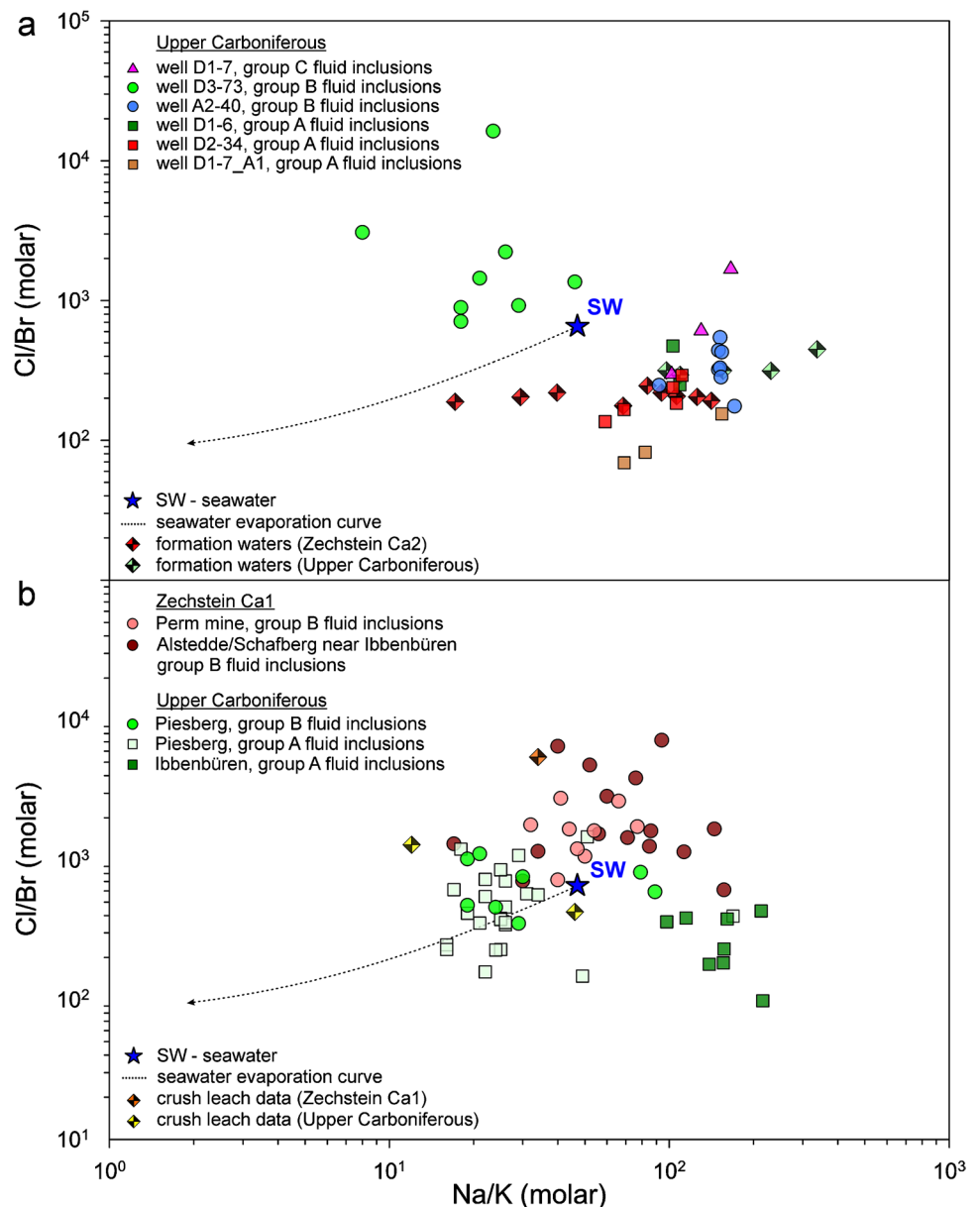
and H$_2$S-rich brine stored in Zechstein carbonates. The bulk crush leach data from the Piesberg block again indicate a seawater evaporation and halite dissolution origin of salinity for fluid inclusions in quartz I and II, respectively (Fig. 12b). Overall it is consistent with the LA-ICP-MS data from individual fluid inclusions (Fig. 12b) however, the advantage of the latter is the possibility to trace the halogen ratios within different FIA's. The bulk crush-leach data also confirms the major trends observed in the distribution of element ratios of fluid inclusions, with a clear compositional distinction between Zechstein-hosted and Upper Carboniferous-hosted fluids (Figs. 12b, 13b).

The halogen data from fluid inclusions in quartz fracture-fillings hosted by Upper Carboniferous strata in the central and southern LSB presented here (Fig. 12) are in excellent

agreement with previous studies of Upper Carboniferous aquifers in the NGB, which suggested that the formation brines stored in the Paleozoic strata, covered by thick Zechstein evaporitic sequence, formed by evaporation of original Paleozoic meteoric water and/or seawater (Lüders et al. 2010). Group A fluid inclusions from both, the central and southern LSB, prove a seawater/water evaporation as the principle source of salinity and are compositionally close to the Upper Carboniferous and Zechstein Ca2 formation waters (Figs. 12, 13). These inclusions yielded the highest fluid temperatures, but salinities lower than halite-saturated seawater of 26 wt% NaCl equiv. (Fig. 4). The hydrothermal group A fluids migrating in the LSB most likely represent the earliest mobilized connate waters derived either from Upper Carboniferous or Zechstein Ca2.
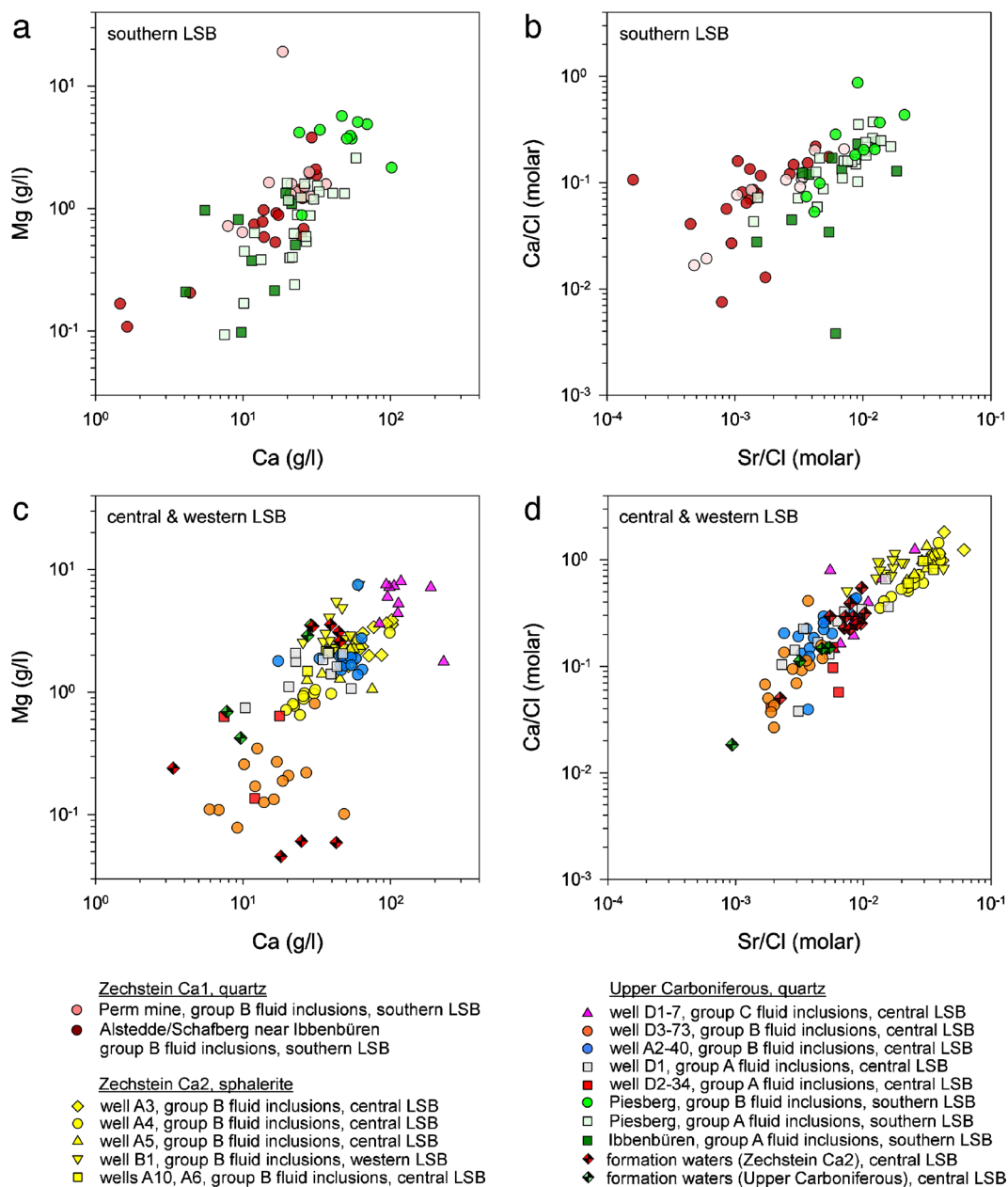
Fig. 14 Plots of Ca vs. Mg concentrations (**a, c**) and Sr/Cl vs. Ca/Cl ratios (**b, d**) of individual sphalerite- and quartz-hosted fluid inclusions from the central, southern and western parts of the Lower Sax-

ony Basin. Data for Upper Carboniferous formation waters are taken from Lüders et al. (2010)

Due to undersaturation with respect to halite, these fluids had a capacity to partly interact with salts in the southern LSB, resulting in a wider spread in Cl/Br ratios extending above the SW value (Fig. 12b).

Water-rock interactions

Analyses of element abundances in FIA's hosted in quartz and sphalerites reveal a variation in the major cation contents (Figs. 13, 14, Fig. 3 in Online Resource 1), which is

indicative of fluid interactions with the basement-sedimentary rock sequence, acting as alternating aquitard and aquifer layers. The highest salinity, group C fluid inclusions, hosted in fracture-filling quartz, plot to the left of the seawater curve in the Na/Br vs. Cl/Br diagram (Fig. 12a) due to Na loss by water-rock interaction (WRI). These fluids are also the most enriched in Ca (Fig. 14c), and may have exchanged Na for Ca through interaction with Ca-rich plagioclase (Lüders et al. 2005), and/or acquired Ca through dolomitization of carbonates. Fracture-filling quartz-hosted, group B fluid

inclusions from sample D3-73 (central LSB), group A FIA's and partly group B FIA's from the Piesberg area (southern LSB) are distinctly enriched in K compared to group A fluid inclusions from the Ibbenbüren area (Fig. 13). This suggests that K was acquired through chemical interaction with K-bearing phases, e.g., potassium feldspar or muscovite, present in sandstones, shales or crystalline basement rocks (de Graaf et al. 2020). Furthermore, all sphalerite-hosted FIAs from Zechstein Ca2, with minor exceptions, have a significant K enrichment relative to the seawater evaporation curve (Fig. 3d in Online Resource 1). This is consistent with enrichment in radiogenic $^{40}Ar^*$ in the sphalerite ore-forming fluids (Fig. 10a). The quartz-hosted group A FIA's from wells D1, D2 and A2 show Na/K ratios closest to values typical of the present-day formation waters in the central LSB (Fig. 13a). Both group B fluid inclusions with salinities that originated by halite dissolution (sample D3-73) as well as group A and B inclusions with salinities attributed to seawater evaporation (Piesberg area) are enriched in K (Fig. 13). This implies that K enrichment in these fluids is not controlled by the fluid type or its origin, instead WRI played a major role in scavenging K from rocks.

Group B fluid inclusions from sample D3-73 are not only enriched in K but also are most intensely depleted in Mg compared to all other FIA's (Figs. 13a, 14c). In contrast, group C inclusions are the least depleted in Mg and the most enriched in Ca (Fig. 14c). This implies that these Ca-Mg-rich brines were not affected by dolomitization, instead they experienced Ca gain with simultaneous Na loss through Na-Ca exchange reactions during albitization of feldspars, as they plot significantly to the left of the SW value (Fig. 12a). The dataset from the Perm Mine as well as sphalerite-hosted FIA's always show general depletion in Mg, with minor exceptions (well B1), and enrichment in Ca relative to the seawater evaporation trajectory (Fig. 3a-b in Online Resource 1). Calcium enrichment of Upper Carboniferous formation waters has been ascribed to dissolution of anorthite and calcite cementing sandstones, whereas Mg depletion to dolomitization and precipitation of Mg-chlorites during diagenesis (Lüders et al. 2010). Depletion of Mg in the fluid, caused by precipitation of diagenetic Mg-chlorite, in fracture-fillings in the Upper Carboniferous strata in both the central (Lüders et al. 2021) and the southern (Wüstefeld et al. 2017) parts of the LSB is a more localized process, therefore widespread dolomitization is likely the major cause. With regard to the trends of Ca and Mg concentrations relative to seawater, the element data, presented here, are consistent with compositions of formation waters (Fig. 3a–b in Online Resource 1). In the southern LSB, all FIA's, except group B fluid inclusions from the Piesberg area, show weak to significant positive correlations between Ca and Mg concentrations as well as between Sr/Cl and Ca/Cl ratios (Fig. 14a–b), which are consistent with

dissolution of carbonates, that contributed to the Ca, Mg and Sr budget of these fluids. Carbonates could have been sourced from the lowermost Zechstein sequence, dolomitic cements or the Devonian carbonate platform, underlying the Carboniferous strata (Wüstefeld et al. 2017; Lüders et al. 2021). In the central LSB, positive trends between Ca and Mg concentrations in quartz- and sphalerite-hosted fluid inclusions, within individual wells, are not observed (Fig. 14c). However, with exception of sphalerite-hosted inclusions from well B1, weak to significant positive correlations between Sr/Cl and Ca/Cl ratios are given for other studied inclusions (Fig. 14c–d). Sphalerite-hosted FIA's have elevated concentrations of Sr compared to Zechstein Ca2 and Upper Carboniferous formation waters, in contrast, quartz-hosted FIA's show Sr concentrations that are similar to data of formation waters (Fig. 14d). These inclusions preserve geochemical characteristics of mixed end-member fluids (metalliferous and Zechstein Ca2-derived H_2S-rich) and thus their Sr signatures are determined by marine Zechstein carbonate and deeper sources. Significant Sr enrichment in sphalerite-hosted FIA's (Figs. 7a, 8, 14d) relative to formation waters indicates that neither Upper Carboniferous nor Zechstein Ca2 formation waters, nor their mixing could have accounted for the bulk Sr budget of the sphalerite-precipitating fluid (Fig. 14d). Therefore, interactions of metalliferous end-member fluids with deeper Sr-rich sources, e.g., crystalline basement and/or Devonian platform carbonates, are required to produce such geochemical signatures.

Ore precipitation conditions

The stable carbon isotope analyses of sphalerite samples reveal variable isotopic compositions of fluid inclusion gases in Zn-Pb ores in different areas of the LSB (Table 1, Fig. 1 in Online Resource 1). The $\delta^{13}C(CH_4)$ values of −7.3 and −6.4‰, and $\delta^{13}C(CO_2)$ values in the range between -9.0‰ and -1.4 (Table 1), measured in fluid inclusion gases from sphalerite in the central part of the LSB, suggest that H_2S was derived by TSR. In contrast, gas-rich inclusions in sphalerite and gangue minerals from the southern and western LSB, show $\delta^{13}C_{CH4}$ values in the range between −26.3 and −24.6‰, which are similar to $\delta^{13}C_{CH4}$ values of *in situ* expelled Upper Carboniferous, coal-derived, dry gas (see also Sośnicka and Lüders, 2020) (Table 1, Fig. 1 in Online Resource 1). Sphalerite from the western LSB contains abundant secondary inclusions and there is evidence of multiple late gas pulses in fracture-filling fluorite, therefore the inclusion gases likely represent the compositions of late post-mineralization gas migration. In the southern LSB, the alteration of hydrocarbon gases was not a major contributor to the isotopic signatures of the fluid inclusion methane in sphalerite or quartz from the Perm Mine. The proximity of coal mines and isotopically unaltered inclusion

gas signatures suggest that only late pulses of hydrocarbon gases were detected. In this light, the Zn-Pb ores from the Perm Mine could have formed by mixing of metal-rich fluids with Zechstein Ca1-derived brines enriched in SO_4^{2-}, which was supplied by dissolution of the Werra anhydrite (A1) and rapidly reduced by hydrocarbons. However, the presence of H_2S pools in now eroded younger Zechstein Ca2 unit cannot not be ruled out, a priori, at the southern flank of the LSB.

Hydrothermal pyrites, hosted in carbonate fracture-fillings in the Zechstein Ca2 unit, from the northern border of the central LSB, show distinct zoning (Fig. 9a–b) and contain PbS inclusions within growth zones (Fig. 9c). The zonation yields cyclic compositional variations in the ore fluid leading to variable concentrations of Pb in the pyrite structure (Fig. 9d–e). The youngest pyrite generation (Py III) has less negative $\delta^{34}S$ values compared to the earlier pyrite II generation (Fig. 9d). This indicates that the ore-stage pyrite formation occurred at different stages of TSR. Pyrite II is more enriched in Pb and has more variable Pb concentrations compared to later pyrite III. There is no clear correlation between Pb concentrations and $\delta^{34}S$ values measured in a traverse, or individual spots (Fig. 9d). This suggests that sulfur and metals were not carried in the same fluid, instead mixing of at least two different fluids must have occurred. An abruptly increasing scatter of fluid inclusion salinities and temperatures in sphalerites, and in quartz intergrown with Zn-Pb ore from the Perm Mine, close to the contact between the Upper Carboniferous and Zechstein (Fig. 5–6), supports fluid mixing as the ore precipitation mechanism within the Zechstein units.

Conclusions

Trace element geochemistry, halogen and noble gas data from fluid inclusions hosted in sphalerites and fracture-filling quartz from Zechstein as well as Upper Carboniferous strata in the LSB, indicate that near-neutral, oxidized ore-forming fluids, derived by sea/water evaporation, evolved towards more reduced, acidic high-salinity brines. The highly reactive saline fluids acquired their metal content by intense fluid-fluid and fluid-wall rock interactions, from deep Paleozoic sources. The interactions with C_{org}-rich strata (coal seams, black shales) had a considerable impact on the trace and critical element budget as well as the redox state of the metalliferous fluids. Our study shows that trace metal and halogen signatures of fluid inclusions, hosted in sphalerites, are excellent tracers of fluid evolution and fluid-wall rock interactions in sedimentary basin settings. The scientific findings of this case study can be extrapolated to similar deep-seated, sediment-hosted base metal ore-forming systems worldwide. Based on our new geochemical and isotopic study it can be concluded:

1) The hydrothermal ore-forming fluids in the LSB were primarily derived by evaporation of either Paleozoic meteoric waters or Zechstein seawater. During progressive burial, the former fluids were modified and converted to formation waters that were subsequently stored in restricted compartments of the Upper Carboniferous sedimentary pile, which developed during structural reorganization at the flanks of the LSB.

2) Dissolution of Permian salt or mixing with halite-dissolution brines significantly contributed to the ore-forming processes in the southern LSB, whereas in the central LSB, fluids which predominantly originated from seawater evaporation were responsible for deposition of deep-seated ores. This is consistent with the asymmetric basin inversion as the more uplifted and exposed Zechstein unit of the southern flank was more vulnerable to penetration of fluids dissolving evaporites, compared to the northern flank, where the deep-seated Zechstein unit has been prevented from significant incursions of fluids from halite dissolution.

3) Enrichment of radiogenic noble gases and potassium in the sphalerite-forming fluids is reported for both the central and southern LSB and is ascribed to intense interactions with the Paleozoic siliciclastic sedimentary and basement rocks.

4) A reflux of the modified, more reducing Zn-Pb-bearing, high-salinity, acidic brines, ascending along structurally controlled pathways, into sour gas and/or sour gas-saturated brine pools hosted by Zechstein Ca2 carbonates, resulted in precipitation of meter-thick Zn-Pb ore zones through mixing and addition of TSR-derived H_2S in the central and western LSB.

5) Mixing processes as well as the origin of H_2S are strongly supported by the element compositions of fluid inclusions and Zechstein Ca2 formation waters, as well as *in situ* stable sulfur and carbon isotopic signatures of ore-stage pyrite and sphalerite-hosted inclusion gases, respectively. The incursion of K-rich, acidic brines along with sulfide ore deposition in the Zechstein Ca2 unit, contributed to dissolution of host carbonates.

6) Less evolved acidic, K-rich brines with a much more pronounced halite-dissolution component, precipitated Zn-Pb ores of the Perm Mine in the southern LSB, however, the origin of H_2S in this area is not entirely clear. It could have been generated through reduction of dissolved sulfate, from Werra anhydrite (A1), by coal-derived hydrocarbons.

7) The timing of the Zn-Pb ore formation in the southern and central LSB can be constrained to the Cretaceous basin inversion.

Declarations

Conflict of interest The authors declare no competing interests.

References

Arndt NT, Fontboté L, Hedenquist JW et al (2017) Future Glob Miner Resour Geochem Persp 6:1–171. https://doi.org/10.7185/geochempersp.6.1

Baldschuhn R, Binot F, Fleig S, Kockel F (2001) Geotektonischer Atlas von Nordwestdeutschland und dem deutschen Nordsee-Sektor. Schweizerbart, Stuttgart, Strukturen, Strukturentwicklung, Paläogeographie

Ballentine CJ, Burgess R, Marty B (2002) Tracing Fluid Origin, Transport and Interaction in the Crust. Rev Mineral Geochem 47:539–614. https://doi.org/10.2138/rmg.2002.47.13

Ballentine CJ, Burnard PG (2002) Production, Release and Transport of Noble Gases in the Continental Crust. Rev Mineral Geochem 47:481–538. https://doi.org/10.2138/rmg.2002.47.12

Banks DA, Giuliani G, Yardley BWD, Cheilletz A (2000) Emerald mineralisation in Colombia: fluid chemistry and the role of brine mixing. Mineral Deposita 35:699–713. https://doi.org/10.1007/s001260050273

Bazarkina EF, Pokrovski GS, Hazemann J-L (2014) Structure, stability and geochemical role of palladium chloride complexes in hydrothermal fluids. Geochim Cosmochim Acta 146:107–131. https://doi.org/10.1016/j.gca.2014.09.024

Benek R, Kramer W, McCann T et al (1996) Permo-Carboniferous magmatism of the Northeast German Basin. Tectonophysics 266:379–404. https://doi.org/10.1016/S0040-1951(96)00199-0

Betz D, Führer F, Greiner G, Plein E (1987) Evolution of the Lower Saxony basin. Tectonophysics 137:127–170

Bodnar RJ (1993) Revised equation and table for determining the freezing point depression of H_2O-NaCl solutions. Geochim Cosmochim Ac 57:683–684. https://doi.org/10.1016/0016-7037(93)90378-A

Bookhagen B, Bastian D, Buchholz P et al (2020) Metallic resources in smartphones. Res Policy 68:101750. https://doi.org/10.1016/j.resourpol.2020.101750

Borg G, Piestrzyński A, Bachmann GH et al (2012) An overview of the European Kupferschiefer deposits. Econ Geo Spec Pub Spec Publication:455–486

Breitkreuz C, Geissler M, Schneider J, Kiersnowski H (2008) Basin initiation: Volcanism and sedimentation. In: Littke R, Bayer U, Gajewski D, Nelskamp S (eds) Dynamics of Complex Intracontinental Basins. The Central European Basin System, Springer, Berlin, pp 173–180

Brink HJ, Dürschner H, Trappe H (1992) Some aspects of the late and post-Variscan development of the Northwestern German Basin. Tectonophysics 207:65–95. https://doi.org/10.1016/0040-1951(92)90472-I

Burisch M, Walter BF, Wälle M, Markl G (2016) Tracing fluid migration pathways in the root zone below unconformity-related hydrothermal veins: Insights from trace element systematics of individual fluid inclusions. Chem Geol 429:44–50. https://doi.org/10.1016/j.chemgeo.2016.03.004

Carpenter AB, Trout ML, Pickett EE (1974) Preliminary Report on the Origin and Chemical Evolution of Lead-and Zinc-Rich Oil Field Brines in Central Mississippi. Econ Geol 69:1191–1206. https://doi.org/10.2113/gsecongeo.69.8.1191

Cook NJ, Ciobanu CL, Pring A et al (2009) Trace and minor elements in sphalerite: A LA-ICPMS study. Geochim Cosmochim Ac 73:4761–4791. https://doi.org/10.1016/j.gca.2009.05.045

Cooke D, Bull S, Large R, McGoldrick P (2000) The Importance of Oxidized Brines for the Formation of Australian Proterozoic-Stratiform Sediment-Hosted Pb-Zn (Sedex) Deposits. Econ Geol 95:1–18. https://doi.org/10.2113/gsecongeo.95.1.1

Crowe DE, Vaughan RG (1996) Characterization and use of isotopically homogeneous standards for in situ laser microprobe analysis of $^{34}S/^{32}S$ ratios. Am Mineral 81:187–193. https://doi.org/10.2138/am-1996-1-223

de Graaf S, Lüders V, Banks DA et al (2020) Fluid evolution and ore deposition in the Harz Mountains revisited: isotope and crush-leach analyses of fluid inclusions. Mineral Deposita 55:47–62. https://doi.org/10.1007/s00126-019-00880-w

Desanois L, Lüders V, Niedermann S, Trumbull RB (2019) Formation of epithermal Sn-Ag-(Zn) vein-type mineralization at the Pirquitas deposit, NW Argentina: Fluid inclusion and noble gas isotopic constraints. Chem Geol 508:78–91. https://doi.org/10.1016/j.chemgeo.2018.04.024

Ding T, Valkiers S, Kipphardt H et al (2001) Calibrated sulfur isotope abundance ratios of three IAEA sulfur isotope reference materials and V-CDT with a reassessment of the atomic weight of sulfur. Geochim Cosmochim Acta 65:2433–2437. https://doi.org/10.1016/S0016-7037(01)00611-1

Drozdzewski G, Dölling M (2018) Elemente der Osning-Störungszone (NW-Deutschland) – Leitstrukturen einer Blattverschiebungszone. Scriptum online Geowissenschaftliche Arbeiten aus Nordrhein-Westfalen Geologischer Dienst NRW 7:1–39

Duschl F, van den Kerkhof A, Sosa G et al (2016) Fluid inclusion and microfabric studies on Zechstein carbonates (Ca2) and related fracture mineralizations – New insights on gas migration in the Lower Saxony Basin (Germany). Mar Pet Geol 77:300–322. https://doi.org/10.1016/j.marpetgeo.2016.06.020

Field JD, Appold MS, Coveney RM, Bodnar RJ (2020) Geochemical characteristics of trace occurrences of Mississippi Valley-type mineralization in the U.S. mid-continent: Implications for deposit growth. J Geochem Explor 213:106514. https://doi.org/10.1016/j.gexplo.2020.106514

Foltyn K, Bertrandsson Erlandsson V, Zygo W et al (2022) New perspective on trace element (Re, Ge, Ag) hosts in the Cu-Ag Kupferschiefer deposit, Poland: Insight from a LA-ICP-MS

trace element study. Ore Geol Rev 143:104768. https://doi.org/10.1016/j.oregeorev.2022.104768

Geological Map of Germany 1:1,000,000 OneGeology-Europe (GK1000-1GE) (WMS), (2018). https://gdk.gdi-de.org/geonetwork/srv/api/records/908b2f4f-5b3a-47cb-9b40-6f76c9db5389

Graedel TE, Gunn G, Espinoza LT (2014) Metal resources, use and Criticality. In: Critical Metals Handbook. John Wiley & Sons, Ltd, pp 1–19

Graupner A (1971) Unterirdische Lagerstätten. In: Behr H-J (ed) Der Landkreis Osnabrück- Geschichte und Gegenwart. Osnabrück, Osnabrück, pp 32–41

Guillong M, Meier DL, Allan MM et al (2008) SILLS: A MATLAB-based program for the reduction of laser ablation ICP-MS data of homogeneous materials and inclusions. Mineralogical Association of Canada, Short Course Series, pp 328–333

Günther D, Audétat A, Frischknecht R, Heinrich CA (1998) Quantitative analysis of major, minor and trace elements in fluid inclusions using laser ablation–inductively coupled plasmamass spectrometry. J Anal At Spectrom 13:263–270. https://doi.org/10.1039/A707372K

Hagemann W (1930) Bergbau- und Hüttenbetriebe des Osnabrücker Landes in ihrer wirtschaftlichen Entwicklung: ein Beitrag zur Wirtschaftsgeschichte Niedersachsens. Selbstverl. der Ges, Hannover

Harms F-J (1984) Perm. In: Klassen H (ed) Die Geologie des Osnabrücker Berglandes. Naturwissenschaftliches Museum, Osnabrück, p 672

Heinrich CA, Pettke T, Halter WE et al (2003) Quantitative multi-element analysis of minerals, fluid and melt inclusions by laser-ablation inductively-coupled-plasma mass-spectrometry. Geochim Cosmochim Acta 67:3473–3497. https://doi.org/10.1016/S0016-7037(03)00084-X

Hoggard MJ, Czarnota K, Richards FD et al (2020) Global distribution of sediment-hosted metals controlled by craton edge stability. Nat Geosci 13:504–510. https://doi.org/10.1038/s41561-020-0593-2

Höll R, Kling M, Schroll E (2007) Metallogenesis of germanium—A review. Ore Geol Rev 30:145–180. https://doi.org/10.1016/j.oregeorev.2005.07.034

Jochum KP, Verma SP (1996) Extreme enrichment of Sb, Tl and other trace elements in altered MORB. Chem Geol 130:289–299. https://doi.org/10.1016/0009-2541(96)00014-9

Jochum KP, Weis U, Stoll B et al (2011) Determination of Reference Values for NIST SRM 610–617 Glasses Following ISO Guidelines. Geostand Geoanal Res 35:397–429. https://doi.org/10.1111/j.1751-908X.2011.00120.x

Kendrick MA, Burgess R, Leach D, Pattrick RAD (2002a) Hydrothermal Fluid Origins in Mississippi Valley-Type Ore Districts: Combined Noble Gas (He, Ar, Kr) and Halogen (Cl, Br, I) Analysis of Fluid Inclusions from the Illinois-Kentucky Fluorspar District, Viburnum Trend, and Tri-State Districts, Midcontinent United States. Econ Geol 97:453–469. https://doi.org/10.2113/gsecongeo.97.3.453

Kendrick MA, Burgess R, Pattrick RAD, Turner G (2002b) Hydrothermal Fluid Origins in a Fluorite-Rich Mississippi Valley-Type District: Combined Noble Gas (He, Ar, Kr) and Halogen (Cl, Br, I) Analysis of Fluid Inclusions from the South Pennine Ore Field, United Kingdom. Econ Geol 97:435–451. https://doi.org/10.2113/gsecongeo.97.3.435

Kennedy BM, Torgersen T, van Soest MC (2002) Multiple atmospheric noble gas components in hydrocarbon reservoirs: a study of the Northwest Shelf, Delaware Basin, SE New Mexico. Geochim Cosmochim Acta 66:2807–2822. https://doi.org/10.1016/S0016-7037(02)00883-9

Knorsch M, Nadoll P, Klemd R (2020) Trace elements and textures of hydrothermal sphalerite and pyrite in Upper Permian (Zechstein) carbonates of the North German Basin. J Geochem Explor 209:106416. https://doi.org/10.1016/j.gexplo.2019.106416

Kockel F (2003) Inversion structures in Central Europe - Expressions and reasons, an open discussion. Neth J Geosci 82:351–366. https://doi.org/10.1017/S0016774600020187

Kucha H (1982) Platinum-group metals in the Zechstein copper deposits, Poland. Econ Geol 77:1578–1591. https://doi.org/10.2113/gsecongeo.77.6.1578

Kucha H, Przybyłowicz W (1999) Noble metals in organic matter and clay-organic matrices, Kupferschiefer, Poland. Econ Geol 94:1137–1162. https://doi.org/10.2113/gsecongeo.94.7.1137

Laurent O, Guillong M, Heinrich CA et al (2021) Advantages of a fast-scanning quadrupole for LA-ICP-MS analysis of fluid inclusions. J Anal At Spectrom 36:2043–2050. https://doi.org/10.1039/D1JA00193K

LBEG Landesamt für Bergbau, Energie und Geologie, Deutschland Report 2014, Erdöl und Erdgas in der Bundesrepublik Deutschland 2013, (2014). www.lbeg.niedersachsen.de. Deutschland

Leach DL, Sangster DF, Kelley KD et al (2005) Sediment-hosted lead-zinc deposits: a global perspective. In: Hedenquist JW, Thompson JFH, Goldfarb RJ, Richards JP (eds) 100th Anniversary Volume (1905-2005). Society of Economic Geologists, pp 561−607. https://doi.org/10.5382/AV100.18

Lecumberri-Sanchez P, Bouabdellah M, Zemri O (2018) Transport of rare earth elements by hydrocarbon-bearing brines: Implications for ore deposition and the use of REEs as fluid source tracers. Chem Geol 479:204–215. https://doi.org/10.1016/j.chemgeo.2018.01.010

Lippolt HJ, Weigel E (1988) 4He diffusion in 40Ar-retentive minerals. Geochim Cosmochim Acta 52:1449–1458. https://doi.org/10.1016/0016-7037(88)90215-3

Lüders V, Plessen B, di Primio R (2012) Stable carbon isotopic ratios of CH_4-CO_2-bearing fluid inclusions in fracture-fill mineralization from the Lower Saxony Basin (Germany) – A tool for tracing gas sources and maturity. Mar Pet Geol 30:174–183. https://doi.org/10.1016/j.marpetgeo.2011.10.006

Lüders V, Plessen B, Romer RL et al (2010) Chemistry and isotopic composition of Rotliegend and Upper Carboniferous formation waters from the North German Basin. Chem Geol 276:198–208. https://doi.org/10.1016/j.chemgeo.2010.06.006

Lüders V, Reutel C, Hoth P et al (2005) Fluid and gas migration in the North German Basin: fluid inclusion and stable isotope constraints. Int J Earth Sci (Geol Rundsch) 94:990–1009. https://doi.org/10.1007/s00531-005-0013-2

Lüders V, Schoenherr J, Sośnicka M et al (2021) Origin, migration pathways, and prediction of high carbon dioxide accumulations in the Lower Saxony Basin (northwestern Germany): Part I. AAPG Bull 105:1909–1945. https://doi.org/10.1306/03122120031

Mamyrin BA, Tolstikhin LN (1984) Helium Isotopes in Nature. Elsevier

Maystrenko Y, Bayer U, Brink H-J, Littke R (2008) The Central European Basin System – an Overview. In: Littke R, Bayer U, Gajewski D, Nelskamp S (eds) Dynamics of Complex Intracontinental Basins. The Central European Basin System, Springer, Berlin, pp 17–34

McCaffrey MA, Lazar B, Holland HD (1987) The evaporation path of seawater and the coprecipitation of Br^- and K^+ with halite. J Sediment Res 57:928–937. https://doi.org/10.1306/212F8CAB-2B24-11D7-8648000102C1865D

Mei Y, Etschmann B, Liu W et al (2015) Palladium complexation in chloride- and bisulfide-rich fluids: Insights from ab initio molecular dynamics simulations and X-ray absorption spectroscopy. Geochim Cosmochim Acta 161:128–145. https://doi.org/10.1016/j.gca.2015.04.009

Nadoll P, Rehm M, Duschl F et al (2018) REY and Trace Element Chemistry of Fluorite from Post-Variscan Hydrothermal Veins in Paleozoic Units of the North German Basin. Geosciences 8:283. https://doi.org/10.3390/geosciences8080283

Nadoll P, Sośnicka M, Kraemer D, Duschl F (2019) Post-Variscan structurally-controlled hydrothermal Zn-Fe-Pb sulfide and F-Ba mineralization in deep-seated Paleozoic units of the North German Basin: A review. Ore Geol Rev 106:273–299. https://doi.org/10.1016/j.oregeorev.2019.01.022

Niedermann S, Bach W, Erzinger J (1997) Noble gas evidence for a lower mantle component in MORBs from the southern East Pacific Rise: Decoupling of helium and neon isotope systematics. Geochim Cosmochim Ac 61:2697–2715. https://doi.org/10.1016/S0016-7037(97)00102-6

Niedermann S, Eugster O (1992) Noble gases in lunar anorthositic rocks 60018 and 65315: Acquisition of terrestrial krypton and xenon indicating an irreversible adsorption process. Geochim Cosmochim Acta 56:493–509. https://doi.org/10.1016/0016-7037(92)90147-B

Peryt TM, Geluk MC, Mathiesen A et al (2010) Zechstein. In: Doornebal JC, Stevenson AG (eds) Petroleum Geological Atlas of the Southern Permian Basin Area. EAGE Publications, Houten, pp 123–147

Pettke T, Oberli F, Audétat A et al (2012) Recent developments in element concentration and isotope ratio analysis of individual fluid inclusions by laser ablation single and multiple collector ICP-MS. Ore Geol Rev 44:10–38. https://doi.org/10.1016/j.oregeorev.2011.11.001

Piestrzyński A, Pieczonka J, Głuszek A (2002) Redbed-type gold mineralisation, Kupferschiefer, south-west Poland. Mineral Deposita 37:512–528. https://doi.org/10.1007/s00126-002-0256-9

Pinti DL, Marty B (1998) The origin of helium in deep sedimentary aquifers and the problem of dating very old groundwaters. Geol Soc Lond, Spec Publ 144:53–68. https://doi.org/10.1144/GSL.SP.1998.144.01.05

Plessen B, Lüders V (2012) Simultaneous measurements of gas isotopic compositions of fluid inclusion gases (N2, CH4, CO2) using continuous-flow isotope ratio mass spectrometry. Rapid Commun Mass Spectrom 26:1157–1161. https://doi.org/10.1002/rcm.6201

Richard A, Banks DA, Mercadier J et al (2011) An evaporated seawater origin for the ore-forming brines in unconformity-related uranium deposits (Athabasca Basin, Canada): Cl/Br and δ37Cl analysis of fluid inclusions. Geochim Cosmochim Acta 75:2792–2810. https://doi.org/10.1016/j.gca.2011.02.026

Röhrs H (1992) Erz und Kohle : Bergbau und Eisenhütten zwischen Ems und Weser. Ibbenbürener Vereinsdruckerei, Ibbenbüren

Schlöglova K, Wälle M, Heinrich CA (2017) LA-ICP-MS analysis of fluid inclusions: contamination effects challenging micro-analysis of elements close to their detection limit. J Anal At Spectrom 32:1052–1063. https://doi.org/10.1039/C7JA00022G

Schoenherr J, Lüders V (2022) Geological risk characterization of traps and migration pathways for gas in an inverted salt basin. Mar Pet Geol 140:105641. https://doi.org/10.1016/j.marpetgeo.2022.105641

Schoenherr J, Lüders V, Leupold M et al (2021) Origin, migration pathways, and prediction of high carbon dioxide accumulations in the Lower Saxony Basin (northwestern Germany): Part II. AAPG Bull 105:1947–1971. https://doi.org/10.1306/03122120032

Schwab G (1985) Paläomobilität der Norddeutsch-Polnischen Senke. Dissertation. Akademie der Wissenschaften der DDR

Senglaub Y, Brix MR, Adriasola AC, Littke R (2005) New information on the thermal history of the southwestern Lower Saxony Basin, northern Germany, based on fission track analysis. Int J Earth Sci 94:876–896. https://doi.org/10.1007/s00531-005-0008-z

Seo JH, Guillong M, Aerts M et al (2011) Microanalysis of S, Cl, and Br in fluid inclusions by LA–ICP-MS. Chem Geol 284:35–44. https://doi.org/10.1016/j.chemgeo.2011.02.003

Sośnicka M, Lüders V (2019) Super-deep, TSR-controlled Phanerozoic MVT type Zn-Pb deposits hosted by Zechstein-2 gas reservoir carbonate (Ca2), Lower Saxony Basin, Germany. Chem Geol 508:62–77. https://doi.org/10.1016/j.chemgeo.2018.04.025

Sośnicka M, Lüders V (2020) Fluid inclusion evidence for low-temperature thermochemical sulfate reduction (TSR) of dry coal gas in Upper Permian carbonate reservoirs (Zechstein, Ca2) in the North German Basin. Chem Geol 534:119453. https://doi.org/10.1016/j.chemgeo.2019.119453

Sośnicka M, Lüders V (2021) Phase transitions in natural C-O-H-N-S fluid inclusions - implications for gas mixtures and the behavior of solid H2S at low temperatures. Nat Commun 12:6975. https://doi.org/10.1038/s41467-021-27269-6

Steele-MacInnis M, Lecumberri-Sanchez P, Bodnar RJ (2012) HokieFlincs_H2O-NaCl: A Microsoft Excel spreadsheet for interpreting microthermometric data from fluid inclusions based on the PVTX properties of H2O–NaCl. Comput Geosci 49:334–337. https://doi.org/10.1016/j.cageo.2012.01.022

Sterner SM, Hall DL, Bodnar RJ (1988) Synthetic fluid inclusions. V. Solubility relations in the system NaCl–KCl–H2O under vapor-saturated conditions. Geochim Cosmochim Acta 52:989–1006

Stoffell B, Appold MS, Wilkinson JJ et al (2008) Geochemistry and Evolution of Mississippi Valley-Type Mineralizing Brines from the Tri-State and Northern Arkansas Districts Determined by LA-ICP-MS Microanalysis of Fluid Inclusions. Econ Geol 103:1411–1435. https://doi.org/10.2113/gsecongeo.103.7.1411

Stuart FM, Burnard PG, Taylor R, Turner G (1995) Resolving mantle and crustal contributions to ancient hydrothermal fluids: He-Ar isotopes in fluid inclusions from Dae Hwa W-Mo mineralisation. South Korea Geochimica et Cosmochimica Acta 59:4663–4673

Stuart FM, Turner G (1992) The abundance and isotopic composition of the noble gases in ancient fluids. Chem Geol 101:97–109. https://doi.org/10.1016/0009-2541(92)90207-L

Tagirov BR, Baranova NN, Zotov AV et al (2013) The speciation and transport of palladium in hydrothermal fluids: Experimental modeling and thermodynamic constraints. Geochim Cosmochim Acta 117:348–373. https://doi.org/10.1016/j.gca.2013.03.047

Torgersen T, Kennedy BM (1999) Air-Xe enrichments in Elk Hills oil field gases: role of water in migration and storage. Earth Planet Sci Lett 167:239–253. https://doi.org/10.1016/S0012-821X(99)00021-7

Van Wees J-D, Stephenson RA, Ziegler PA et al (2000) On the origin of the Southern Permian Basin, Central Europe. Mar Pet Geol 17:43–59. https://doi.org/10.1016/S0264-8172(99)00052-5

Viets JG, Hofstra AH, Emsbo P (1996) Solute Compositions of Fluid Inclusions in Sphalerite from North American and European Mississippi Valley-Type Ore Deposits: Ore Fluids Derived from Evaporated Seawater. https://doi.org/10.5382/SP.04.35

Whitehouse MJ (2013) Multiple Sulfur Isotope Determination by SIMS: Evaluation of Reference Sulfides for Δ33S with Observations and a Case Study on the Determination of Δ36S. Geostand Geoanal Res 37:19–33. https://doi.org/10.1111/j.1751-908X.2012.00188.x

Wilkinson JJ, Stoffell B, Wilkinson CC et al (2009) Anomalously Metal-Rich Fluids Form Hydrothermal Ore Deposits. Sci 323:764–767. https://doi.org/10.1126/science.1164436

Wüstefeld P, Hilse U, Lüders V et al (2017) Kilometer-scale fault-related thermal anomalies in tight gas sandstones. Mar Pet Geol 86:288–303. https://doi.org/10.1016/j.marpetgeo.2017.05.015

Yardley BWD, Bodnar RJ (2014) Fluids in the Continental Crust. Geochem Persp 3:1–127. https://doi.org/10.7185/geochempersp.3.1

Ziegler AM (1990) Phytogeographic patterns and continental configurations during the Permian Period. Geol Soc Lond Mem 12:363–379. https://doi.org/10.1144/GSL.MEM.1990.012.01.35

Ziegler PA (1977) Geology and hydrocarbon provinces of the North Sea. GeoJournal 1:7–32